Nature Communications

https://doi.org/10.1038/s41467-026-73280-0

Article in Press

Acetylated mitochondrial MDH2 regulates CTR2 transcription to induce cuproptosis during *Escherichia coli* infection

Received: 28 November 2025

Accepted: 7 May 2026

Cite this article as: Wang, H., Xiao, P., Chen, L. *et al.* Acetylated mitochondrial MDH2 regulates CTR2 transcription to induce cuproptosis during *Escherichia coli* infection. *Nat Commun* (2026). https://doi.org/10.1038/s41467-026-73280-0

Hao Wang, Peng Xiao, Liping Chen, Meng Zhou, Jingsong Zhang, Jinlong Xiao, Ru Zhao, Jingang Zhao, Tianling Pan, Jue Sheng, Yue Li, Jinzhi Ma, Longbao Lv, Yulin Yan & Hong Gao

Acetylated mitochondrial MDH2 regulates CTR2 transcription to induce cuproptosis during *Escherichia coli* infection

Hao Wang,[1, #] Peng Xiao,[2, #] Liping Chen,[3, #] Meng Zhou,[1] Jingsong Zhang,[2] Jinlong Xiao,[2] Ru Zhao,[2] Jingang Zhao,[4] Tianling Pan,[2] Jue Sheng,[2] Yue Li,[2] Jinzhi Ma,[2] Longbao Lv,[5, *] Yulin Yan,[2, *] and Hong Gao[2,4, *]

[1]College of Food Science and Technology, Yunnan Agricultural University, Kunming 650201, China.

[2]College of Veterinary Medicine, Yunnan Agricultural University, Kunming 650201, China.

[3]College of foreign languages, Yunnan Agricultural University, Kunming 650201, China.

[4]Faculty of Animal Science and Technology, Yunnan Agricultural University, Kunming 650201, China.

[5]National Resource Center for Non-Human Primates, National Research Facility for Phenotypic & Genetic Analysis of Model Animals (Primate Facility), Kunming Institute of Zoology, Chinese Academy of Sciences, Kunming 650107, China.

[#]These authors contributed equally: Hao Wang, Peng Xiao, Liping Chen.

*Correspondence：Hong Gao (gaohongping@163.com), Yulin Yan (yanyulin333@163.com), Longbao Lv (lvlongbao@mail.kiz.ac.cn),

Abstract

Pathogenic bacteria frequently manipulate host cell death pathways to facilitate infection, though the precise mechanisms remain elusive. Here, we demonstrate that pathogenic *Escherichia coli* disrupts copper homeostasis through upregulation of copper transporter CTR2, thereby triggering cuproptosis to drive infectious pathology. During infection, circulating lipopolysaccharide activates the morphological hallmarks of cuproptosis via the gut–LPS–liver axis. Furthermore, mitochondrial malate dehydrogenase 2 (MDH2) functions as a transcriptional regulator, triggering CTR2 expression and metabolic reprogramming via acetylation-dependent nuclear translocation in response to infection. Notably, inhibiting cuproptosis mitigates liver damage caused by infection, highlighting its critical role in pathogen-host interactions. These findings identify a mechanism underlying *E. coli* pathogenesis and support therapeutic approaches based on targeted modulation of metal-dependent cell death.

Introduction

Pathogenic *Escherichia coli* (*E. coli*) infection represents a widespread global public health challenge 1,2. The effects of *E. coli* result from its ability to undermine host immunity and trigger programmed cell death (PCD), with outcomes ranging from self-limiting gastroenteritis to life-threatening sepsis 3. While PCD may help contain pathogen spread, excessive cell death exacerbates tissue injury, and the molecular basis of this duality remains poorly understood 4-6. A similar duality is observed in the regulation of copper, an essential trace element. Copper can be mobilized by immune cells as an antimicrobial effector, yet dysregulated copper homeostasis provokes cytotoxicity 7-9. Therefore, a critical balance in the regulation both of PCD and the cellular copper level underlies the host response to pathogenic *E. coli* infection.

Cuproptosis is a recently identified form of copper-dependent programmed cell death characterized by the aggregation of lipoylated mitochondrial proteins, particularly dihydrolipoamide S-acetyltransferase (DLAT) 10. This process suppresses the lipoylation of mitochondrial enzymes such as DLAT and DLST, leads to the loss of iron–sulfur (Fe–S) cluster proteins (e.g., FDX1), and triggers an acute proteotoxic stress response 11. These features suggest a link between metal homeostasis and infection-associated pathology. However, how bacterial pathogens leverage infection-induced copper dysregulation to provoke cuproptosis in host cells remains unclear. While the interplay between *E. coli* and host immune defenses has been extensively characterized, the connection between infection induced copper dysregulation and cuproptosis remains a critical gap in understanding.

Copper transporters (CTRs) lie at the heart of cellular copper balance, with CTR1 mediating uptake in response to dynamic changes in copper availability 12,13. During pathogenic assaults, bioavailable copper levels rise systemically or at infection sites 7,14,15. Salmonella disrupts intracellular copper homeostasis by upregulating CTR1 and ATP7b 8,16, and the *E. coli* virulence factor LPS induces CTR1 to promote copper accumulation in immune cells 17. In stark contrast, the role of CTR2 in infection-driven copper homeostasis remains enigmatic.

Here, we sought to further characterize the mechanism by which pathogenic *E. coli* infection manipulates cuproptosis in host cells, including the potential role of CTR2 in this process. Our results show that *E. coli* infection selectively upregulates CTR2 to induce copper overload and cuproptosis. Furthermore, mitochondrial malate dehydrogenase 2 (MDH2), a tricarboxylic acid (TCA) cycle enzyme, undergoes acetylation-dependent nuclear translocation and directly binds the CTR2 promoter to regulate its transcription. These findings redefine host–pathogen dynamics through metal-dependent cell death and reveal a pivotal transcriptional role for MDH2 with potential implications for therapeutic development.

Results

E. coli infection induces cuproptosis in host cells

To investigate the relationship between pathogenic *Escherichia coli* (*E. coli*) infection and cuproptosis, we established an *E. coli* infection model in mice (Supplementary Fig. 1a). At approximately 9 h post-infection, the copper and iron levels in the livers of the mice significantly increased, followed by a decrease at 24–36 h post-infection (Fig. 1a, Supplementary Fig. 1b). Given that elevated copper levels may induce cuproptosis, we next examined FDX1 expression, an essential regulator of cuproptosis 18,19. Both the mRNA and protein levels of FDX1 in the livers of infected mice decreased within 24 h of *E. coli* infection (Figs. 1b, c). This suggests that cuproptosis may be induced during *E. coli* infection.

To identify the molecular mechanisms underlying *E. coli*-induced cuproptosis, we performed RNA-seq analysis of the liver, followed by KEGG enrichment analysis, which revealed that cuproptosis-related pathways, including the TCA cycle and pyruvate metabolism 20, were significantly involved in the infection response (Supplementary Fig. 1c). Moreover, the expression levels of iron-sulfur cluster proteins (e.g., *FDX1*, *DPYD*, *NDUFB10*, *NDUFB8*), TCA cycle enzymes (e.g., *DLAT*, *PDHA1*, *ACO2*, *SDHB*, P*DHB*), metal ion metabolism-related proteins (e.g., *STEAP1-4*, *SOD*), and copper ion metabolism pathway proteins (e.g., *CCS*, *SLC31A2*) exhibited significant fluctuations following infection (Fig. 1d), which confirms the activation of hallmark cuproptosis-associated gene expression 10. Western blot analysis confirmed that *E. coli* infection promotes the loss of iron-sulfur cluster proteins and reduced mitochondrial abundance (TOMM20), inhibited DLAT lipoylation, and induced DLAT oligomerization in mouse liver at 18 h post-infection (Fig. 1e).

To further elucidate how pathogenic bacteria induce cuproptosis in host cells, we established an *in vitro* model in which cells were infected with *E. coli*. To mimic the high-copper environment observed post *E. coli* infection, we selected a $CuCl_2$ concentration (5 μM) that is non-toxic to both cells and *E. coli* (Supplementary Fig. 1d, Fig. 1f). The addition of $CuCl_2$ 5 minutes after infection exacerbated the cellular damage and death triggered by *E. coli* (Figs. 1g-i, Supplementary Fig. 1e). Furthermore, the intracellular copper levels significantly increased only under the combined condition of infection and copper addition, whereas copper alone did not produce this effect (Fig. 1j, Supplementary Fig. 1f). Interestingly, *E. coli* infection alone upregulated *FDX1* mRNA levels, yet FDX1 expression markedly decreased when copper was added (Fig. 1k). Similarly, neither

$CuCl_2$ nor *E. coli* infection alone induced loss of iron-sulfur cluster proteins, inhibition of DLAT lipoylation, or DLAT aggregation; these hallmarks of cuproptosis were observed only under combined treatment (Fig. 1l, Supplementary Fig. 1g), with effects detectable as early as 3 hours post-infection (Supplementary Fig. 1h). Additionally, immunofluorescence analysis corroborated these findings, with prominent DLAT foci observed under infection-plus-copper conditions but rarely observed in cells treated with copper alone (Fig. 1m). To rule out interference from other PCD pathways, we pretreated cells with inhibitors of pyroptosis, ferroptosis, necroptosis, autophagy, and the copper chelator TTM (tetrathiomolybdate). Only TTM effectively mitigated the cellular damage induced by the combination of *E. coli* and $CuCl_2$ (Fig. 1n). Although *E. coli* infection alone can engage pyroptosis, apoptosis and ferroptosis, elevating copper availability preferentially unmasked the defining features of copper-dependent cuproptosis, consistent with the obligate copper requirement of this pathway (Fig. 1o). Similar results were observed in various cells such as primary mouse hepatocytes (PMHs), HeLa and HEK293T, indicating that this mechanism is not cell-type specific (Fig. 1p, q). Collectively, these results confirm that pathogenic *E. coli* disrupts host copper ion homeostasis, promotes excessive copper accumulation, and ultimately triggers cuproptosis.

E. coli upregulates CTR2 to disrupt intracellular copper homeostasis

Copper uptake largely depends on copper transporters (CTRs) 13,21. To determine whether *E. coli* perturbs host copper homeostasis by modulating CTR expression, we analyzed CTR transcription after infection. RNA-seq and GO enrichment analysis of copper metabolism-related genes revealed significant upregulation of *SLC31A2* (CTR2) (Supplementary Fig. 2a), a low-affinity copper importer 22. Further investigation showed that *E. coli* infection upregulates CTR2 expression in mouse livers while downregulating the high-affinity copper transporter CTR1 (*SLC31A1*) (Figs. 2a, Supplementary Fig. 2b). To determine the effect of $CuCl_2$ post-infection, we additionally evaluated CTR1/CTR2 expression in HepG2 cells. In the absence of $CuCl_2$, *E. coli* infection increased both CTR1 and CTR2 expression, however, with the addition of 5 μM $CuCl_2$, only CTR2 remained upregulated (Fig. 2b, Supplementary Fig. 2c), suggesting a pivotal role for CTR2 in high-copper environments post-infection. Moreover, infection-associated copper enrichment suppressed CTR1 expression, consistent with recent studies showing that elevated copper levels inhibit CTR1 transcription via activated NF-***κ***B 23. To define the role of CTR2 in copper influx, we assessed its subcellular localization following infection. CTR2 was detected in both lysosomal and plasma membrane fractions, and infection significantly increased its abundance in the plasma membrane fraction (Fig. 2c). We then labeled live cells with Sulfo-NHS-SS-biotin, followed by membrane fractionation, anti-CTR2 immunoprecipitation, and western blot analysis. These experiments confirmed successful enrichment of CTR2 in the membrane fraction (Supplementary Fig. 2d, left). Streptavidin probing of the same samples identified a specific band at the expected molecular weight of CTR2, and this signal was further enhanced after infection (Supplementary Fig. 2d, right). Collectively, these findings support a model in which *E. coli* infection enhances copper influx and disrupts intracellular copper homeostasis by promoting CTR2 enrichment at the plasma membrane.

To verify the role of CTR2, we overexpressed human CTR2 (OE-hCTR2) in HepG2 or HeLa cells. Overexpression alone had minimal effects; however, after 3 hours of $CuCl_2$ exposure, the cells exhibited swelling, reduced viability, and significant intracellular copper accumulation, which was alleviated by copper chelation with TTM (Figs. 2d–e, Supplementary Fig. 2e). Concurrently, OE-hCTR2 cells exposed to 1 μM $CuCl_2$ displayed DLAT aggregation, loss of iron-sulfur cluster proteins, and inhibition of DLAT lipoylation (Fig. 2f, Supplementary Fig. 2f). To assess CTR2's impact on copper homeostasis during infection in vivo, we also established a mouse model with liver-specific CTR2 overexpression using rAAV (Fig. 2g, Supplementary Fig. 2g). After *E. coli* infection, these mice showed enhanced hepatic copper accumulation, reduced expression of iron-sulfur cluster proteins (e.g., FDX1), and inhibited DLAT lipoylation (Fig. 2h, Supplementary Fig. 2h–i). Histological analysis indicated that CTR2 overexpression also exacerbated *E. coli*-induced liver cell damage, cell death, and infiltration of the inflammatory cytokine IL-1β, suggesting heightened inflammation (Supplementary Fig. 2j–k). To validate the function of CTR2, we generated CTR1 and CTR2 knockout HepG2 cells using CRISPR/Cas9 (Supplementary Fig. 3a–b). CTR2 knockout markedly alleviated infection-induced copper imbalance, DLAT aggregation, iron-sulfur cluster protein loss, and cuproptosis, whereas CTR1 knockout had negligible effects on copper homeostasis and cuproptosis (Figs. 2i-j, Supplementary Fig. 3c–d). Collectively, these findings demonstrate that *E. coli* infection selectively upregulates CTR2, disrupting intracellular copper homeostasis and triggering cuproptosis (Fig. 2k).

While the morphological features of various PCD types, such as ferroptosis 24 and pyroptosis 25, are well-defined, those of cuproptosis remain largely uncharacterized. Thus, to characterize cuproptosis cellular morphology, we first observed the aggregation of DLAT in hCTR2-OE cells by confocal imaging. An abundance of DLAT foci were formed in response to $CuCl_2$, which was similar to the effect of treatment with the classic cuproptosis inducer elesclomol (ES) (Fig. 2l). Given that cuproptosis primarily occurs in mitochondria, we further analyzed the mitochondrial morphology using transmission electron microscopy. ES-treated and hCTR2-OE cells displayed increased mitochondrial density, compaction, darker staining, reduced or absent cristae, a significant decrease in mitochondrial numbers, and a notable rise in abnormal or damaged mitochondria accompanied by autophagosome formation, with no apparent changes in other organelles (Figs. 2m–o). Mitochondrial examination further confirmed a reduction in mitochondrial abundance and an increase in Mito-SOX signal in both groups, indicating mitochondrial damage and a marked elevation in oxidative stress levels (Fig. 2p, Supplementary Fig. 3e-f). Finally, scanning electron microscopy and fluorescence imaging further revealed numerous bubble-like protrusions on the cell surface of ES-treated and hCTR2-OE cells, increasing in number and size over time (Fig. 2q, Figs. 3a-b). These morphological features are clearly distinct from those of pyroptosis and ferroptosis; we therefore designate the observed structures "cuproptotic bodies." The identification of cuproptotic bodies provides additional ultrastructural evidence that CTR2 overexpression drives cuproptosis and helps elucidate the cellular basis of *E. coli* associated pathology.

The "gut-LPS-liver axis" regulation in *E. coli* induced cuproptosis

The intestine is the primary site most affected by *E. coli* infection 26. Therefore, we evaluated the effects of *E. coli* on cuproptosis in the gut. Copper and iron levels in the mouse intestine sharply increased 3 hours after infection (Fig. 4a, Supplementary Fig. 4a). Furthermore, the aggregation of DLAT and a loss of iron-sulfur cluster proteins were observed in the intestine at 3 hours and in the liver at 6 hours post-infection (Figs. 4b–d). Moreover, the tight junction barrier in the intestine was severely damaged at 18 h post-infection, which could be replicated in cultured IPEC-J2 cells (Supplementary Fig. 4b). To investigate potential regulatory mechanisms, we performed high-throughput sequencing of the mouse gut microbiome. Functional annotation using FAPROTAX revealed that infection led to an increased abundance of microbial communities associated with human pathogens (Supplementary Fig. 4c). Furthermore, LEfSe analysis indicated a significant rise in the abundance of Gram-negative bacteria, including *Escherichia flexneri*, *Escherichia dysenteriae*, and *Helicobacter pylori BU*, following *E. coli* infection (Fig. 4e). PICRUSt2 functional analysis further suggested that the functions of the microbiota after infection were enriched in lipopolysaccharide biosynthesis, the TCA cycle and pyruvate metabolism (Fig. 4f). Consistently, LPS levels in the serum and liver of infected mice were significantly elevated (Fig. 4g). Correlation analysis demonstrated a strong positive association between the abundance of *Escherichia flexneri* and *Escherichia dysenteriae* and LPS concentrations in the blood and liver (r^2 = 0.87 and 0.854) (Supplementary Fig. 4d–e), suggesting that these bacteria may be key contributors to elevated LPS levels.

To confirm the role of the gut microbiome in inducing cuproptosis, we generated pseudo-germ-free mice using an antibiotic cocktail (ABX) and introduced the microbiome from infected mice into ABX mice via fecal microbiota transplantation (FMT) 27,28 (Fig. 4h, Supplementary Fig. 4f). (Successful ABX establishment was confirmed by the enlarged cecum in mice 29). Compared to normal mice, ABX mice exhibited a significant reduction in liver cuproptosis after infection, whereas FMT-treated ABX mice showed renewed DLAT aggregation (Fig. 4i). Additionally, FMT mice displayed more severe intestinal villus breakage compared to ABX mice, as well as spleen and liver enlargement (Fig. 4j, Supplementary Fig. 4g–h), accompanied by marked liver function impairment and an inflammatory cytokine storm (Fig. 4j, Supplementary Fig. 4i–l). Notably, ABX-treated mice infected with *E. coli* displayed lower circulating LPS levels than infected mice with an intact microbiota, indicating that gut microbiota dysbiosis substantially contributes to the systemic endotoxin burden during infection. This conclusion was further supported by fecal microbiota transplantation, which increased LPS levels in ABX-treated mice (Fig. 4k; Supplementary Fig. 4m).

To determine whether LPS triggers cuproptosis, we pretreated cells with LPS, followed by combined stimulation with $CuCl_2$. LPS treatment alone caused cells to swell and become rounded, while treatment with LPS + $CuCl_2$ resulted in bubble-like protrusions on the cell surface (Supplementary Fig. 5a). ICP-MS analysis further revealed that LPS significantly elevates the cellular copper content (Supplementary Fig. 5b), leading to DLAT aggregation and the formation of numerous DLAT foci (Fig. 4l). To assess the impact of LPS on hepatic cuproptosis in vivo, polymyxin B/E (Poly B/E), a potent LPS neutralizer 30, was administered subcutaneously to mice

immediately after LPS treatment. Poly B/E reduced CTR2 expression and suppressed DLAT oligomerization (Supplementary Fig. 5c). Further investigation showed that, similar to *E. coli* infection, LPS treatment alone upregulated the expression of copper transporters CTR1 and CTR2; however, under combined LPS and $CuCl_2$ treatment, only CTR2 expression remained elevated, triggering cuproptosis (Fig. 4m). This finding was further validated in CTR1/2 knockout cells (Fig. 4m, Supplementary Fig. 5d). Scanning electron microscopy and fluorescence analysis also confirmed that the combination of LPS and $CuCl_2$ induced the formation of typical cuproptotic bodies (Supplementary Fig. 5e-f). Collectively, these findings demonstrate that *E. coli* infection induces liver cuproptosis by regulating the "gut-LPS-liver" axis.

Mitochondrial MDH2 regulates CTR2 promoter activity

To investigate the mechanism by which *E. coli* infection upregulates CTR2 to trigger cuproptosis, we constructed a yeast one-hybrid library using HepG2 cDNA, with the CTR2 promoter as bait for genome-wide screening (Fig. 5a, Supplementary Data 1). KEGG enrichment analysis revealed that candidate regulatory factors were predominantly associated with metabolic pathways, including the TCA cycle and pyruvate metabolism (Supplementary Fig. 6a). Subsequently, PCR array analysis of all candidate genes in the liver of *E. coli*-infected mice identified six infection-related genes (*NME2*, *DDX49*, *RPL13A*, *RPL3*, *NPM1*, and *MDH2*), with *MDH2* exhibiting the most significant upregulation (Fig. 5b). MDH2, a mitochondrial malate dehydrogenase, is conventionally associated with metabolic functions 31. Thus, to determine whether MDH2 directly binds to the CTR2 promoter, we confirmed the interaction using yeast point-to-point one-hybrid assays (Fig. 5c). Microscale thermophoresis (MST) analysis with purified MDH2 protein and CTR2 promoter fragments also demonstrated that MDH2 directly binds to the CTR2 promoter DNA sequence, with a dissociation constant (Kd) of 0.62 μM (Fig. 5d, Supplementary Data 2). In vivo dual-luciferase reporter assays further validated that MDH2 binds to and regulates CTR2 promoter activity (Fig. 5e). ChIP–qPCR with primer sets spanning the core promoter fragments identified in the screen localized MDH2 binding specifically to the p3 fragment, showing robust enrichment relative to adjacent regions and IgG/input controls (Fig. 5f, Supplementary Fig. 6b). Because transcription factor functionality depends on nuclear localization, we examined the subcellular distribution of MDH2 after combined LPS and $CuCl_2$ treatment. When cells were treated with $CuCl_2$ alone, MDH2 was still confined to mitochondria, while the addition of LPS induced its partial translocation to the nucleus, a phenomenon also observed in the livers of *E. coli*-infected, LPS-injected, and FMT mice (Figs. 5g–h, Supplementary Fig. 6c). Nuclear-cytoplasmic fractionation and western blot analysis further confirmed that LPS treatment enabled MDH2 nuclear entry (Supplementary Fig. 6d), suggesting that MDH2 acquires nuclear localization capability under stress conditions.

To elucidate the mechanism by which MDH2 regulates CTR2 expression, we generated MDH2-overexpressing and knockout cells (Supplementary Fig. 6e-f) and treated them with $CuCl_2$ following LPS or PBS pretreatment (Fig. 5i). The results demonstrate that neither MDH2 overexpression alone nor $CuCl_2$ treatment alone altered CTR2 expression, intracellular copper levels, or iron-sulfur cluster protein stability. However, when the cells were pretreated with LPS,

MDH2 overexpression significantly enhanced CTR2 expression, promoted copper accumulation, and resulted in the loss of iron-sulfur cluster proteins (Figs. 5j-k, Supplementary Fig. 6f). Further analysis showed that MDH2 overexpression alone did not elevate *SLC31A2* transcription. However, in the presence of LPS, *SLC31A2* transcription was markedly upregulated and further amplified by MDH2 overexpression (Fig. 5l), indicating that MDH2 exerts transcriptional regulation of CTR2 only under LPS-induced conditions. Moreover, neither MDH2 overexpression nor LPS treatment alone was sufficient to induce DLAT aggregation or trigger cuproptosis. However, combining LPS with MDH2 overexpression significantly increased CTR2 expression and induced cuproptosis (Figs. 5m–n), an effect that was reversed in MDH2 knockout cells (Figs. 5o–p). Furthermore, the copper chelator TTM effectively suppressed this process (Fig. 5q, Supplementary Fig. 6g). Collectively, these data support a model in which *E. coli* infection induces the translocation of MDH2 from mitochondria to the nucleus approximately 1 h post infection, where MDH2 binds to the CTR2 promoter and activates its transcriptional expression (~2 h), thereby disrupting intracellular copper homeostasis and initiating copper toxicity and cuproptosis between 3 and 5 h after infection (Supplementary Fig. 6h-i).

Acetylation drives MDH2 nuclear translocation and metabolic reprogramming

Previous studies have shown that the acetylation of selected proteins promotes nuclear translocation [32,33]. To investigate whether acetylation may serve as the molecular mechanism by which bacterial pathogen infection facilitates the nuclear translocation of MDH2, we examined overall acetylation levels in mouse livers and HepG2 cells. Both *E. coli* infection and LPS treatment increased the overall levels of acetylation modification (Fig. 6a, Supplementary Fig. 7a). Moreover, the acetylation levels of both exogenous and endogenous MDH2 were increased after LPS treatment (Fig. 6b). Subsequent acetyl-proteomics analysis, three lysine residues of MDH2 (K297, K301, and K329) were identified as sites with significantly increased acetylation (Figs. 6c–e and Supplementary Fig. 7b, Supplementary Data 3). To further assess the MDH2 acetylome, we mutated these lysine residues to arginine. Consistent with the acetylome findings, mutations at all three residues dramatically decreased MDH2 acetylation (Supplementary Fig. 7c–d). Importantly, these sites are highly conserved across humans, mice, rats, and pigs (Supplementary Fig. 7e), which supports their putative biological role.

Protein acetylation relies on the dynamic balance between histone acetyltransferases (HATs) and histone deacetylases (HDACs) [34-36]. To elucidate the mechanism of MDH2 acetylation, we reanalyzed RNA-seq data from mouse livers and observed no significant changes in the expression of GNAT and MYST family HAT members. However, among the HDAC family, Sirt3, and HDAC5/8/11 exhibited significant regulation post-infection (Fig. 6f), suggesting that MDH2 acetylation may be primarily regulated by HDACs. In cells treated with Trichostatin A (TSA), a broad-spectrum inhibitor of the HDAC family deacetylases, and Nicotinamide (NAM), an inhibitor of SIRT family deacetylases, combined TSA and NAM treatment enhanced MDH2 acetylation. However, strong MDH2 acetylation was detected only in cells treated with NAM alone (Fig. 6g). To identify the specific SIRT family member regulating MDH2 acetylation, we knocked down Sirt1-7 in HepG2 cells and assessed MDH2 acetylation. Knockdown of Sirt3, but not other

deacetylases, significantly increased the basal acetylation level of MDH2 (Supplementary Fig. 8a). Furthermore, *E. coli* infection reduced Sirt3 expression (Supplementary Fig. 8b), and high MDH2 acetylation levels were observed in both Sirt3 knockdown and 3-TYP (a Sirt3 inhibitor)-treated cells (Fig. 6h). Subsequent GST-pulldown assays confirmed that Sirt3 interacts with MDH2 (Fig. 6i), further supporting the possibility that Sirt3 may inhibit MDH2 acetylation via deacetylation. Notably, 3-TYP treatment promoted MDH2 nuclear translocation in cells, with similar results observed in the livers of 3-TYP-treated mice (Figs. 6j-k, Supplementary Fig. 8c). Furthermore, both Sirt3 knockdown and 3-TYP treatment enhanced MDH2 nuclear localization and upregulated CTR2, thereby triggering cuproptosis (Figs. 6l–m). To assess whether acetylation sites of MDH2 are required for its nuclear translocation, MDH2-deficient cells were transfected with either MDH2-WT or an acetylation-defective mutant (MDH2-Mut[3KR]). Nuclear–cytoplasmic fractionation showed that MDH2 was detected in the nucleus only in cells expressing MDH2-WT, but not MDH2-Mut[3KR]. Notably, increased CTR2 abundance and DLAT oligomerization were observed exclusively upon MDH2-WT expression (Supplementary Fig. 8d). In contrast, TTM inhibited cell death induced by 3-TYP combined with $CuCl_2$ (Supplementary Fig. 8e-f), supporting a model in which Sirt3 loss driven MDH2 acetylation promotes nuclear translocation, CTR2 upregulation, and copper-dependent cell death.

Given that TLR4 is a canonical cell-surface receptor for LPS [37], we generated TLR4-knockout cells (Supplementary Fig. 9a). TLR4 deficiency mitigated the LPS-induced reduction in Sirt3 expression and suppressed MDH2 acetylation (Fig. 6n, Supplementary Fig. 9b). Critically, TLR4 knockout reduced CTR2 expression and the incidence of cuproptosis (Fig. 6o, Supplementary Fig. 9c). Consistently, TLR4 knockdown in PMHs blunted LPS-driven CTR2 upregulation and diminished the expression of cuproptosis-associated markers (Supplementary Fig. 9d). Collectively, these results indicate that pathogen infection or LPS stimulation impairs MDH2 deacetylation via the TLR4–Sirt3 axis, thereby promoting MDH2 nuclear translocation and ultimately driving cuproptosis (Supplementary Fig. 9e).

Metabolic reprogramming is a key adaptive mechanism for hosts to resist infection [38-40], with acetylation playing a pivotal role in metabolic regulation [41-43]. Consistently, acetylomics analysis of the liver revealed that *E. coli* infection induced acetylation of 143 mitochondrial proteins, with KEGG enrichment indicating that these targets are primarily enriched in the TCA cycle and pyruvate metabolism, including key enzymes such as DLAT, IDH1/2, MDH1/2, and ACO1/2 (Supplementary Fig. 10a–c). Targeted metabolomics analysis of energy metabolism showed that post-infection, levels of Acetyl-CoA, Citrate, Cis-Aconitate, Isocitrate, and α-Ketoglutarate in the TCA cycle were upregulated, while Succinyl-CoA and Succinate were downregulated (Figs. 6p–q, Supplementary Fig. 10d). Concurrently, the anti-inflammatory metabolite Itaconic acid was sharply increased (Supplementary Fig. 10d), suggesting that metabolic reprogramming may serve dual roles in anti-infection and regulation of the cell fate. Furthermore, multi-omics analysis indicated that these metabolite changes were predetermined by alterations in the mRNA levels of related genes (Supplementary Fig. 10e). Enzyme activity assays further corroborated these findings by verifying that in the early stages of infection, the activities of mMDH, CS and SDH in mouse livers increased, while PDH, IDH activity decreased, which aligns with the dynamics of

TCA cycle metabolites (Fig. 6r). Interestingly, LPS treatment also induced partial nuclear translocation of ACO2, SDHA, and CS (Supplementary Fig. 10f). Collectively, these data demonstrate that *E. coli* infection promotes the acetylation of key metabolic enzymes via LPS-TLR4 engagement, driving global reprogramming of energy metabolism in vivo.

Inhibition of cuproptosis alleviates *E. coli* induced liver injury

Finally, to assess the in vivo role of cuproptosis in the host's defense against *E. coli* infection, we pretreated mice with TTM and infected wild-type (WT) and $CTR2^{-/-}$ mice with *E. coli* (Fig. 7a). TTM pretreatment significantly improved the survival rate of WT mice and reduced the bacterial load in their livers. Although the bacterial load was also reduced in the livers of $CTR2^{-/-}$ mice, the observed survival benefit did not reach statistical significance (Figs. 7b–c). Furthermore, TTM suppressed the infection-induced surge in hepatic copper levels (Fig. 7d), and the subsequent occurrence of cuproptosis (Fig. 7e, Supplementary Fig. 11a). Importantly, TTM treatment attenuated hepatomegaly, histological liver injury, and decline in hepatic function. It also suppressed the hepatic cytokine storm and inhibited activation of the TLR4/NF-κB inflammatory signaling pathway. These effects were recapitulated in $CTR2^{-/-}$ mice (Figs. 7f–i, Supplementary Fig. 11b–d). Notably, both TTM intervention and CTR2 deficiency alleviated infection-induced splenomegaly (Supplementary Fig. 11e), suggesting that copper chelation plays a role in the systemic regulation of the immune response. Critically, TTM treatment also attenuated the infiltration of neutrophils and macrophages, as well as the activation of macrophages, caused by the infection (Fig. 7j), implying that infection-triggered cuproptosis may extend beyond parenchymal hepatocytes. We therefore examined cuproptosis in immune cells and found that both HepG2 cells and RAW264.7 macrophages displayed similar cuproptotic markers upon treatment with *E. coli* plus $CuCl_2$, indicating that cuproptosis also occurs in infiltrating immune cells and may contribute to the observed hepatic pathology (Supplementary Fig. 11f). In summary, our findings demonstrate that TTM-mediated inhibition of cuproptosis plays a crucial role in preventing *E. coli*-induced liver damage through bacterial suppression and inflammation modulation.

Discussion

While copper homeostasis is fundamental to cellular function, its role in bacterial pathogenesis and regulated cell death has not been well characterized 9. In this study, we found that mitochondrial MDH2 acts as a transcription factor, upregulating CTR2 expression through acetylation-dependent nuclear translocation. Assisted by the "gut-LPS-liver axis," MDH2 participates in *E. coli*-induced disruption of copper homeostasis and cuproptosis, driving the pathological progression of infection (Fig. 8). Although our in vitro model required copper supplementation to robustly induce cuproptosis, this strategy was designed to recapitulate the copper overload observed in vivo after infection. Both in vivo and in vitro systems consistently demonstrate that CTR2 upregulation is required to initiate the downstream cascade of hallmark cuproptosis events, underscoring the central role of this pathway in infection pathology. Whereas copper is traditionally viewed as an antibacterial weapon deployed by immune cells 7,8, *E. coli* appears to hijack the host’s endogenous copper regulatory machinery, redirecting host defense

toward pathological cell death. The core of this conversion lies in the upregulation of CTR2 and abnormal copper uptake, triggering cuproptosis. This mechanism differs fundamentally from how Salmonella maintains copper balance by regulating CTR1 and ATP7b [8,16] highlighting the diversity of bacterial strategies to evade copper-mediated defenses. These findings also resolve the long-standing paradox of copper's dual role in immunity and cytotoxicity and redefine the metabolic crosstalk between host and pathogen during infection.

Copper overload is known to activate the NF-κB pathway, promoting inflammatory responses [44-46], while copper chelators can inhibit LPS-induced inflammation and NF-κB activity [47,48]. Recent evidence indicates that combined LPS and copper stimulation activates the NF-κB subunit p65, which in turn suppresses CTR1 transcription via negative feedback 23, consistent with our observation of CTR1 downregulation under high-copper conditions following infection. We show that *E. coli* subverts the host copper-regulatory network via CTR2, converting the antibacterial copper response into a “Trojan horse” that precipitates cell death. Although a high-copper microenvironment at infection sites can restrict pathogen proliferation [14,49], CTR2-mediated copper influx can exceed cellular tolerance, driving aggregation of lipoylated mitochondrial proteins and causing collateral “friendly fire” damage to host tissues. By inducing cuproptosis, *E. coli* compromises barrier integrity and facilitates dissemination. In our study, copper chelation with TTM attenuated both the inflammatory storm and hepatic cuproptosis induced by *E. coli*, supporting copper modulation as a potential therapeutic strategy for liver injury. However, whether the upregulation of CTR2 represents an adaptive strategy for bacteria that serves to deplete host extracellular copper and evade immune surveillance requires further investigation.

This study also confirms the regulatory role of the "gut-LPS-liver axis" in the systemic propagation of cuproptosis. *E. coli* infection leads to the enrichment of pathogenic Enterobacteriaceae and elevated circulating LPS levels, resulting in endotoxemia and hepatic copper and iron overload, directly enhancing the CTR2-mediated copper influx and DLAT aggregation. Although FMT reproduced LPS-driven liver injury, it remains unclear whether bacterial effectors other than LPS directly regulate CTR2. LPS is a well-known immune activator that upregulates CTR1 to stimulate copper uptake in immune cells 17. Its involvement in CTR2 mediated, copper dependent cell death also highlights a previously unrecognized aspect of host-pathogen interactions.

An intriguing finding lies in the secondary transcriptional regulatory function of mitochondrial MDH2. Though MDH2 functions as a classical mitochondrial metabolic enzyme 50, we demonstrated that it also translocates to the nucleus upon acetylation to transcriptionally activate CTR2. This finding expands the repertoire of metabolic enzymes with dual regulatory capabilities. Although several metabolic enzymes, including MDH2, exhibit nuclear localization, their functional outputs diverge depending on cellular fate decisions [31,51,52], with GAPDH and IMPDH demonstrating transcriptional roles under specific cellular states [53,54]. Therefore, future research to characterize the effect of various cellular states on MDH2-dependent CTR2 expression would be of interest. While prior research identified MDH2 as a cytoplasmic RNA-binding protein regulating sodium channel Scn1a expression 55, the preesent study reveals that MDH2 employs a SIRT3-regulated acetylation mechanism for nuclear entry and binds the CTR2 promoter DNA with

competitive binding affinity (*Kd* = 0.62 μM) to activate transcription. This unveils sophisticated metabolic adaptation that coordinates with metal homeostasis. Because MDH2 lacks an obvious DNA-binding domain, we suggest that stress-induced acetylation may expose a cryptic DNA-interacting surface; a subset of MDH2 then accumulates in the nucleus and directly associates with the CTR2 promoter. This behavior is reminiscent of other moonlighting enzymes, including GAPDH and IMPDH. Although cofactors may stabilize or contextualize this interaction in vivo, the direct binding measured here supports MDH2 as a primary effector of CTR2 transcription in this setting. Determining the structural basis of acetylation-enabled DNA engagement remains an important goal. At present, our multidimensional evidence indicates that the transcriptional regulatory function of MDH2 depends on acetylation-mediated nuclear translocation. We also acknowledge that future studies using nucleus-targeted MDH2, such as an NLS-MDH2 fusion construct, will provide further validation of this mechanism. Such metabolism-copper homeostasis crosstalk broadens the scope of transcriptional networking, positioning MDH2 as a critical node in infection-induced cellular responses. These insights compel a re-evaluation of metal dysregulation, not merely as a bystander effect but as a central driver of infectious pathology.

Consistent with our findings, *E. coli* infection has been found to reprogram host metabolism, inducing hyperacetylation of mitochondrial enzymes (e.g., DLAT, IDH1/2) and skewing of the TCA cycle toward citrate and α-ketoglutarate accumulation, creating a metabolic state resembling the "broken TCA cycle" observed in cancer 56. The results of the present work, and those of others, extend this model by reporting a unique convergence of host metabolism with cuproptosis 10. The concurrent nuclear presence of MDH2, ACO2, and CS observed in the present study suggests infection-mediated disruption of compartmentalized metabolism, with stressed metabolic enzymes potentially serving as epigenetic regulators 51. Furthermore, the roles of other metabolic enzymes in infection response and epigenetic regulation warrant further exploration.

Although this study defines a mechanism of *E. coli*-induced cuproptosis, several limitations merit consideration. First, we established that acetylated MDH2 binds the CTR2 promoter to activate transcription, the exact molecular motifs and structural mechanisms governing this interaction remain unresolved. Future investigations should employ CUT&Tag to map chromatin accessibility and identify consensus binding motifs, combined with cryo-electron microscopy to elucidate the structural architecture of the MDH2-DNA complex. Second, while our emphasis on LPS as the principal microbial effector in the gut-liver axis successfully recapitulates key features of hepatic cuproptosis, contributions from additional bacterial components cannot be ruled out. Third, although we established the temporal sequence of MDH2 nuclear translocation, CTR2 induction, copper accumulation, and subsequent cuproptosis, the use of temporally multiplexed imaging would enable real-time visualization of this entire cascade in single living cells and allow a more precise analysis of its dynamic progression.

Methods

Reagents and antibodies

All reagents and antibodies used in this study are listed in Supplementary Data 4.

Mice

C57BL/6 male littermates (7–8 weeks) were obtained from the Kunming Institute of Zoology, Chinese Academy of Sciences (Kunming, Yunnan, China). Only males were used to avoid confounding by estrous cycle and fluctuating estrogen, which modulate inflammation, infection susceptibility, and metabolism. Experiments were performed in specific pathogen-free (SPF) facilities at laboratory animal center, Kunming Institute of Zoology, Chinese Academy of Sciences (Yunnan, China) under standardized conditions: 12-hour light/dark cycle, ambient temperature of 25 ± 2°C, relative humidity of 40 ± 10%, and ad libitum access to food and water. CTR2-deficient (*SLC31A2*$^{-/-}$) mice on a C57BL/6 genetic background were acquired from APxBIO. To generate hepatic CTR2-overexpressing mice (OE-CTR2), recombinant adeno-associated virus (AAV) particles were produced by co-transfecting 293T cells with the packaging plasmid AAV Helper-pDGM6 (Addgene #110660), helper plasmid pAAV2/8 (Addgene #112864), and the rAAV-TBG-mCherry-CTR2 construct. AAV particles were purified using the Universal Virus Concentration Kit (Beyotime #C2901M) and administered via tail vein injection (200 μl/mouse, ~1×10^{11} viral genome copies 57). Mice were euthanized 14 days post-injection, and liver tissues were harvested, embedded in Tissue-Tek OCT compound (Sakura Finetech #4583), snap-frozen in liquid nitrogen, and assessed for mCherry-CTR2 expression via Olympus SpinSR10 confocal microscopy. All procedures complied with national guidelines for laboratory animal welfare and were approved by the Animal Ethics Committee of Yunnan Agricultural University (Approval No. 202303006). The experimental design adhered to the ARRIVE guidelines and the Sex and Gender Equity in Research (SAGER) guidelines for reporting in vivo research.

Cell culture methods and bacterial strains

The following human cell lines were maintained in Dulbecco's Modified Eagle Medium (DMEM) supplemented with 10% fetal bovine serum (Yeasen #40131ES) and 1% penicillin-streptomycin (Yeasen #60162ES) at 37°C with 5% CO_2: HeLa (ATCC CCL-2), A549 (ATCC CCL-185), HepG2 (ATCC HB-8065), IPEC-J2 (BTCC-4025), HEK293T (ATCC CRL-11268), Vero (ATCC CCL-81), RAW264.7 (ATCC TIB-71) and primary mouse hepatocytes (PMHs; isolated from healthy C57BL/6 mice [58,59]). HepG2 knockout cell generation is described in the following section. For DLAT and MDH2 immunofluorescence, cells were incubated with 100 nM MitoTracker Red CM-H2Xros for 25 minutes before fixation.

Pathogenic *E. coli* O157:H7 (ATCC 700728, Shiga toxin gene-deficient), cloning-competent DH5α (Takara #9057), and protein-expression BL21 (Takara #9126) strains were cultured in LB broth with agitation (37°C). Following transformation, DH5α cultures were recovered in SOC medium.

Plasmid constructs and transfection

Mammalian expression vector construction: The *SLC31A2* cDNA derived from HepG2 was cloned into the GFP-tagged pEGFP-C3 vector via *XhoI/KpnI* restriction sites. MDH2 was cloned into the Myc-tagged pcDNA3.1(+)-N-Myc vector using *EcoRI/KpnI* sites. Additionally, MDH2 lysine substitution mutants (K78R, K297R, K301R, K307R, K309R, K335R, 3KR [K297R, K301R,

K329R]) were constructed by Sangon Biotech (Shanghai, China) based on the pcDNA3.1(+)-N-Myc-MDH2[WT] backbone. For in vitro protein expression, MDH2 was excised from pcDNA3.1(+)-N-Myc-MDH2 using *EcoRI/KpnI* and subcloned into pTac-GST-WELQ (generating GST-MDH2) and pCZN1 (generating His-MDH2) vectors (pCZN1 was a gift from Zoonbio). Sirt3 was cloned into pCZN1 via *BamHI/EcoRI* sites. For liver-specific CTR2 overexpression in mice, mouse CTR2 (*SLC31A2*) cDNA was inserted into the rAAV-TBG-mCherry vector (under the liver-specific TBG promoter) using *HindIII* and *BamHI* restriction sites, yielding rAAV-TBG-mCherry-CTR2. Gene knockout vector preparation: CRISPR/Cas9 vectors were constructed using the pSpCas9(BB)-2A-GFP (PX458) backbone (Addgene #48138) 60. sgRNAs targeting CTR1 (gRNA1: 5′-GAGTGTGAGGCTGAAGTGGT-3′), CTR2 (gRNA1: 5′-TTTCATCTTCTCAGATACAG-3′, gRNA2: 5′-GCAGGAGCACCAACACCGAA-3′), MDH2 (gRNA: 5′-GGTGTTGAACAGGTCGTCCC-3′), and TLR4 (gRNA: 5′-TCTCTAGAGAACTTCCCCAT-3′) were designed using CRISPOR (https://crispor.gi.ucsc.edu/crispor.py). Single-strand sgRNA oligonucleotides synthesized by Sangon Biotech (Shanghai, China) were phosphorylated, annealed, and ligated into *BbsI*-digested vectors using T4 ligase. All constructs were validated by Sanger sequencing.

Transfection: Plasmid or siRNA transfection was performed using the GenePulser Xcell system (Bio-Rad). Transfection mixtures (plasmid/siRNA with Engreen Transfection Reagent, #98668) were electroporated into cells under optimized conditions (250 V, 950 μF) following the manufacturer's protocol.

Sirt1-7 and *TLR4* knockdown was performed using shRNA plasmids (pLKO.1; Addgene #10878). Constructs targeting *Sirt1-7* or *TLR4* were transfected into HepG2 cells or PMHs using the GenePulser Xcell system. shRNA oligonucleotides were cloned into pLKO.1 via the *AgeI/EcoRI* sites. The target sequences were as follows: *Sirt1* (GCAAAGCCTTTCTGAATCTAT), *Sirt2* (TATGACAACCTAGAGAAGTAC), *Sirt3* (CCCAACGTCACTCACTACTTT), *Sirt4* (CCCGATTGCAATACTGAACAT), *Sirt5* (GAGTCCAATTTGTCCAGCTTT), *Sirt6* (TGGAAGAATGTGCCAAGTGTA), *Sirt7* (CTTCAGAAAGGGAGAAGCGTT), *TLR4* (GCCATCATTATGAGTGCCAAT). Cells were subjected to experimental treatments 48 hours post-transfection.

Protein expression and purification

The GST-MDH2 fusion protein was expressed in *E. coli* BL21 cells by induction with 0.5 mM IPTG (Sigma-Aldrich, #PHG0010) at 18°C for 24 h. Bacterial pellets were resuspended in pre-chilled lysis buffer supplemented with a protease inhibitor cocktail (1:100; Fitgene, #FI8804). After thorough mixing, cells were lysed by sonication until the lysate became clear. The fusion protein was purified using glutathione-Sepharose 4B beads (GE Healthcare, #17-0756-01) and eluted by incubating the resin with 10 mM reduced glutathione elution buffer (Fitgene, #FI8804) at 4°C for 0.5 h. The eluate was concentrated and desalted to remove reduced glutathione using an Amicon Ultra-4 centrifugal filter (Millipore, #UFC801024), and the purified protein was stored at −80°C in 25% (v/v) glycerol.

His-tagged MDH2 and Sirt3 were separately expressed in *E. coli* BL21 cells induced with 0.5 mM IPTG at 11°C for 24 h. Both proteins were purified using a His-tagged Protein Purification Kit (Beyotime #P2226) following the manufacturer's protocol. Purified His-MDH2 was used for microscale thermophoresis (MST) assays, whereas His-Sirt3 served as the interaction partner for GST-MDH2 in GST pull-down experiments.

In vitro infection

Cells were preconditioned in antibiotic-free medium before bacterial infection. Early stationary-phase bacteria (OD_{600} = 0.8) were pelleted by centrifugation, washed with DPBS, and resuspended. HepG2, HeLa, A549, IPEC-J2, Vero, PMHs and HEK293T cells were challenged with pathogenic *E. coli* (MOI = 20) or LPS (1 μg/ml, *E. coli*-0111:B4) 61.

For copper ion intervention, cells were first infected with *E. coli* (MOI = 20) or treated with LPS for 5 minutes under standard conditions. $CuCl_2$ was then added to the cell-bacteria co-culture medium at defined concentrations. Cellular samples and culture supernatants were collected at predetermined time points for downstream analyses.

Antibiotic cocktail (ABX) treatment

Adult mice received a 4-week oral regimen of a quadruple antibiotic cocktail (ampicillin 1 g/L, vancomycin 0.5 g/L, neomycin 1 g/L, metronidazole 0.5 g/L) in drinking water to deplete gut microbiota, as adapted from 27,29. Antibiotics were administered ad libitum to circumvent oral gavage-induced stress. Solutions were prepared in autoclaved water containing 1% (w/v) sucrose, sterile-filtered (0.22 μm), and replaced thrice weekly. Daily water consumption was recorded, with mice maintaining unrestricted access to standard chow. After completion of the ABX regimen, a subset of mice was euthanized to assess microbiota depletion, and the remaining mice proceeded to infection or fecal microbiota transplantation (FMT) experiments.

Faecal microbiota transplantation (FMT) of ABX-treated mice

FMT was conducted as adapted from fresh fecal samples from healthy donor mice and *E. coli*-infected donors (18 h post-infection) were homogenized in sterile saline (0.9%) 28,62, filtered through sterile mesh, and supplemented with 10% glycerol for cryopreservation. Bacterial viability was confirmed (1×10^8 CFU/mL) prior to administration. After a 3-day washout period following ABX treatment 63, ABX-treated recipient mice received the fecal suspension by oral gavage at 10 μL/g body weight. To enhance colonization, equivalent volumes were applied topically to abdominal and dorsal skin until fur saturation, facilitating microbial transfer through natural grooming behaviors.

In vivo murine infection

C57BL/6 mice (7-8 weeks) were stratified into wild-type (WT), CTR2-overexpressing (OE-CTR2), and CTR2-deficient ($CTR2^{-/-}$) groups. Infection models were established via intraperitoneal injection of *E. coli* (1×10^9 CFU/mouse, suspended in PBS at 1×10^{10} CFU/mL) 64 or LPS (20 mg/kg) 65. For experiments involving ABX mice, the antibiotic regimen was followed by a 3-day washout period to minimize residual antibiotic activity, after which infections were

performed according to the procedures described above. Mice meeting predefined clinical endpoints were euthanized. For survival studies, a higher infectious dose (1×10^{10} CFU) was administered, with mortality assessed at 4-hour intervals. Bacterial loads in tissues were quantified 24 hours post-infection, and survival rates were tracked for 5 days. At designated time points, tissues and blood were collected, and organ indices ([organ wet weight (mg) / body weight (g)] × 100%) were calculated to assess pathological enlargement.

To evaluate TTM's anti-inflammatory effects, mice received TTM (30 mg/kg in drinking water, 3 weeks pre-infection) 47. For 3-TYP pretreatment studies, mice were administered 3-TYP intraperitoneally (50 mg/kg every 48 hours, 1 week pre-infection) 66 to assess MDH2 subcellular localization in the liver. To implement an in vivo LPS-neutralization strategy, mice were administered the potent LPS-neutralizing agent polymyxin B/E (2 mg/kg) by subcutaneous injection immediately after LPS treatment 30. Bacterial colonization and survival rates were analyzed, with euthanasia performed at protocol-defined intervals.

Histological analysis

Liver and intestinal tissues were fixed in 4% paraformaldehyde (24 h), paraffin-embedded, and sectioned (5 μm). Sections underwent dewaxing, rehydration, and hematoxylin & eosin (H&E) staining before resin mounting. Histological imaging was performed using an Olympus BX53 microscope with CellSens software. Immunohistochemistry (IHC): Antigen retrieval was achieved by heating paraffin sections in 0.01 M citrate buffer (pH 6.0, 95°C, 20 min). Endogenous peroxidase activity was blocked with 3% H_2O_2. Sections were incubated overnight at 4°C with primary antibodies (anti-IL-1β, anti-MDH2), washed with PBS, and probed with biotinylated secondary antibodies (Vector Laboratories) at room temperature. Signal detection employed streptavidin-biotin-peroxidase complexes with DAB chromogen. Immunofluorescence: After antigen retrieval, sections were incubated overnight at 4°C with macrophage/neutrophil markers (CD86, F4/80, CD11b), followed by species-matched fluorescent secondary antibodies and DAPI (Yeasen #40728ES03) counterstain. Fluorescent images were acquired using an Olympus BX53 microscope to quantify immune cell infiltration and activation (All experiments were repeated independently at least three times.).

Biochemical analysis in the plasma and tissue

Following euthanasia, blood samples were centrifuged (10,000 × g, 15 min, 4°C) to isolate plasma. Hepatic function was assessed using commercial kits (Nanjing Jiancheng Bioengineering Institute) to quantify plasma aspartate aminotransferase (AST, #C010-2-1) and alanine aminotransferase (ALT, #C009-2-1) following manufacturer instructions. Plasma IL-18 and TNF-α levels were measured using mouse-specific ELISA kits (Jonln #JLW20253, #JLW10484). Serum and hepatic LPS concentrations were quantified using a competitive ELISA kit (Jonln #JL20691). Serum analyzed directly and liver tissues homogenized in PBS (1:9 w/v) before testing. For the assay, samples/standards were loaded onto a 96-well plate coated with an anti-mouse LPS antibody, which recognizes antigenic sites including lipid A, core polysaccharide, and O antigen. After sequential incubation with HRP-conjugated detection reagents and three washes with PBS-T,

colorimetric signals were developed using 3,3',5,5'-tetramethylbenzidine (TMB). Absorbance at 450 nm was measured for analyte quantification.

Immunostaining and confocal microscopy

Cells were incubated with 100 nM MitoTracker Red CM-H2Xros for 25 minutes to label mitochondria before fixation. For indirect immunofluorescence, fixed cells were probed overnight at 4°C with primary antibodies targeting mitochondrial enzymes (DLAT, MDH2, ACO2, SDHA, CS), followed by 1-hour incubation with Alexa Fluor 488/594-conjugated secondary antibodies at room temperature. Nuclei were counterstained with DAPI. Mitochondrial superoxide levels were assessed in cells using MitoSOX Red (5 μM) or MitoTracker Red (100 nM) (25-minute incubation) and Hoechst 33342 nuclear stain (Yeasen #40731ES10). All imaging was performed using a GE IN Cell Analyzer 6000 system equipped with a Nikon 60×/0.95NA objective for high-resolution visualization and quantitative analysis (All experiments were repeated independently at least three times.).

Flow cytometric analysis

Cells were stained with MitoSOX Red (5 μM) or MitoTracker Red (100 nM) for 25 min to assess mitochondrial oxidative stress and mitochondrial content, respectively. Cells were then washed three times with PBS, harvested by gentle scraping on ice, and resuspended in PBS containing 2% FBS and DAPI (1 μg/mL). Dead cells were excluded based on DAPI staining. Data were acquired on a BD LSRFortessa and analyzed using FlowJo v9.9.4 (BD).

ICP-MS

Cellular and tissue copper/iron concentrations were analyzed by inductively coupled plasma mass spectrometry (ICP-MS). Cell pellets were digested in nitric acid (65°C, 1 h) and diluted with ultrapure water. Murine tissue samples (~0.1 g) underwent microwave-assisted digestion in PTFE vessels using HNO_3 (5 mL) and H_2O_2 (1 mL) following distilled water hydration. After 1 h equilibration, samples were processed in a CEM Mars 6 microwave system. All samples were spiked with 50 μL indium internal standard (100 ng/mL). Copper and iron concentrations were determined using a PerkinElmer NexION 1000G ICP-MS under optimized conditions.

Viability and cell proliferation assays

Cellular viability under $CuCl_2$ exposure (1-1000 μM) was assessed using the Cell Counting Kit-8 (CCK-8, Yeasen #40203ES) in basal medium for mammalian cells and *E. coli*, following manufacturer protocols. Post-infection or LPS treatment, residual extracellular bacteria were removed via triple PBS washes containing antibiotics before viability assessment. To dissect cell death pathways, cells were pretreated with TTM (20 μM, copper chelator), Z-VAD-FMK (30 μM, pan-caspase inhibitor), Ferrostatin-1 (10 μM, ferroptosis inhibitor), Necrostatin-1 (20 μM, necroptosis inhibitor), 3-Methyladenine (5 mM, autophagy inhibitor) 10, prior to *E. coli* infection and $CuCl_2$ exposure. Viability was quantified via CCK-8 assays, while lactate dehydrogenase (LDH) release in supernatants was measured using the LDH Cytotoxicity Assay Kit (Yeasen #40209ES). Total cellular LDH (lysate-derived) served as the reference for percentage

calculations. Phase-contrast microscopy (Nikon ECLIPSE SiRS) documented morphological changes (restricted to HeLa cells) to complement cytotoxicity data (All experiments were repeated independently at least three times.).

TEM and SEM

Cells were fixed in 2.5% glutaraldehyde (4°C, overnight), post-fixed with 1% osmium tetroxide in 100 mM phosphate buffer (pH 7.4, 1.5 h, room temperature), and dehydrated through an ethanol gradient. Samples were acetone-cleared, embedded in Eponate 12 resin (Ted Pella), and sectioned (60 nm). Ultrathin sections were stained with 2% uranyl acetate and lead citrate, then analyzed using a Tecnai G2 Spirit Twin TEM for mitochondrial ultrastructure. Glutaraldehyde-fixed cells were dehydrated via ethanol gradient (30–100%), subjected to tert-butanol critical-point drying, and sputter-coated with gold-palladium. Surface morphology was imaged using a JEOL JSM 66390LV field-emission SEM at 10 kV (All experiments were repeated independently at least three times.).

Immunoblot analysis

Cellular and murine tissue samples were lysed in ice-cold RIPA buffer (Yeasen #20114ES60) containing 1× HALT protease inhibitor cocktail (Thermo Fisher Scientific) for 30 min. Lysates were clarified by centrifugation (12,000 × g, 15 min, 4°C), and protein concentrations were quantified using a BCA assay (Yeasen #20201ES). Equal protein aliquots were denatured in 5× SDS-PAGE loading buffer (Yeasen #20315ES) at 95°C for 5 min, separated on 4–12% Bis-Tris gels, and electroblotted onto PVDF membranes. Membranes were blocked with protein-free buffer (Servicebio #G2052), probed with primary antibodies (4°C, overnight), and detected using HRP-conjugated secondary antibodies (1 h, room temperature) with chemiluminescence imaging (Servicebio SCG-W5000). Non-denatured protein samples were solubilized in NativePAGE™ buffer (Invitrogen #BN2003), resolved on NativePAGE™ Bis-Tris gels (Invitrogen #BN1001BOX), and transferred to PVDF membranes. Oligomeric states were assessed via standard immunoblotting. Subcellular fractions (nuclear, cytosolic, lysosomal, and plasma membrane) were isolated using a commercial protein fractionation kit (Beyotime, #P0028; Invent, SM-005 and LY-034) to assess the localization of MDH2 and CTR2. Cells transfected with target plasmids were lysed in TAP buffer (20 mM Tris-HCl pH 7.4, 0.5% NP-40, 150 mM NaCl, 1 mM NaF/Na_3VO_4/EDTA). Lysates were incubated with antibody-conjugated magnetic beads (4°C, overnight), washed, and analyzed by SDS-PAGE/immunoblotting. Cell-surface biotinylation was performed using the Pierce™ Cell Surface Protein Biotinylation and Isolation Kit (Thermo Scientific, A44390) according to the manufacturer's instructions. Briefly, cells were washed with PBS, labeled with Sulfo-NHS-SS-Biotin for 10 min at room temperature, and then washed with ice-cold TBS. Cells were lysed on ice for 30 min in lysis buffer containing protease inhibitors, and the clarified lysates were incubated with NeutrAvidin agarose for 30 min at room temperature. After four washes, bound proteins were eluted with 10 mM DTT for 30 min and subjected to downstream analyses. CTR2 and streptavidin immunoprecipitates were then analyzed by immunoblotting using an anti-CTR2 antibody or streptavidin, respectively (All experiments were repeated independently at least three times.).

In vitro GST pull-down assay and acetylation assay

Purified GST, GST-MDH2, and His-Sirt3 were incubated in NP-40 lysis buffer (4°C, 4 h). Glutathione-sepharose 4B beads were added to the mixture and rotated (4°C, 2 h). After washing with lysis buffer, bound proteins were eluted, separated by SDS-PAGE, and immunoblotted for interaction analysis. HEK293T cells expressing Myc-tagged MDH2 variants (WT, K78R, K297R, K301R, K307R, K329R, K335R,3KR [K297R, K301R, K329R]) were lysed in TAP buffer. Lysates underwent immunoprecipitation (IP) with anti-Myc magnetic beads. Precipitated proteins were resolved by SDS-PAGE and immunoblotted with anti-acetyl-lysine antibody (Ace-lys) to assess site-specific acetylation at lysine residues.

Enzymatic activity assay

Enzymatic activities of citrate synthase (CS), isocitrate dehydrogenase (IDH), succinate dehydrogenase (SDH), malate dehydrogenase (MDH), and pyruvate dehydrogenase (PDH) were quantified using commercial kits: CS (Elabscience #E-BC-K178-M), IDH (Beyotime WST-8-based #S0526S), SDH (Elabscience #E-BC-K649-M), MDH (Beyotime WST-8-based #S0514S), PDH (Elabscience #E-BC-K650-M). Positive controls provided with each kit were analyzed in parallel. All measurements followed manufacturer protocols.

RNA-seq

Murine liver tissues were snap-frozen in liquid nitrogen post-collection. Total RNA was extracted and quality-controlled (RIN $\geq$ 8.0) using an Agilent 2100 Bioanalyzer. Strand-specific RNA libraries (APxBIO) were prepared with the NEBNext Ultra II RNA Library Prep Kit and sequenced on an Illumina NovaSeq 6000 platform (150 bp paired-end reads). Raw reads were processed with Trimmomatic for quality filtering and aligned to the mm10 genome via HISAT2. Gene expression quantification used featureCounts, with differential expression analysis performed in DESeq2 ($|\log_2 FC| \geq 1.3$, adj. $P < 0.05$). Functional annotation of differentially expressed genes (DEGs) included KEGG pathway enrichment and Gene Ontology (GO) classification.

PacBio Sequencing for Gut Microbiome Analysis

Murine colonic fecal samples were snap-frozen in liquid nitrogen immediately post-collection and stored at -80°C. Microbial genomic DNA was extracted using the QIAamp DNA Stool Mini Kit (Qiagen). Lingen Biotech (Shanghai, China) performed PacBio library preparation and full-length 16S rRNA gene sequencing. Raw circular consensus sequencing (CCS) reads were quality-filtered using SMRTLink v9.0. Operational taxonomic units (OTUs) were clustered at 98.65% similarity threshold via UPARSE, followed by chimera removal with UCHIME. Alpha diversity (Shannon/Chao1 indices) and beta diversity (PCoA/PERMANOVA) analyses were conducted. Differential taxa abundance was identified using LEfSe (LDA score >2, $P < 0.05$). Microbial functional potential was inferred via PICRUSt2 using KEGG pathway annotations.

Yeast One-Hybrid Library Screening and Validation

HepG2 cell-derived total RNA was reverse-transcribed into cDNA and cloned into the pGADT7-DEST vector via Gateway® technology (Invitrogen) to generate a yeast one-hybrid cDNA library. Bait sequences targeting specific gene promoters (pCTR2, Supplementary Note 1) were cloned into the pAbAi vector and genomically integrated into Y1HGold yeast strains. Post-autoactivation testing, library screening was performed on SD/-Leu and SD/-Leu + AbA (200 ng/mL) agar plates. Positive clones were validated by Sanger sequencing. For pairwise validation, pGADT7-prey vectors were co-transformed into Y1HGold[pAbAi-Bait] strains. Interactions were verified by growth on selective media, with controls: Positive: pAbAi-p53 + pGADT7-Rec-53, Negative: pAbAi-p53 + empty pGADT7. Technical support was provided by Zoon Biotechnology (Nanjing, China).

qRT-PCR, PCR array and ChIP-qPCR

Total RNA was extracted from tissues and cultured cells using AG RNAex Pro Reagent (Accurate Bio #AG21102). First-strand cDNA synthesis was performed with Hifair® III 1st Strand cDNA Synthesis SuperMix (Yeasen #40203ES), including genomic DNA removal. qRT-PCR assays utilized Hieff UNICON® SYBR Green Master Mix (Yeasen #11184ES), with GAPDH as the endogenous control. Relative gene expression was calculated via the 2^(−ΔΔCt) method, using primers validated by PrimerBank 67. Custom PCR Array Profiling: A QIAGEN custom PCR array was designed to assess yeast one-hybrid-enriched candidates. Liver RNA samples were analyzed on the array, and data were processed using RT² Profiler PCR Data Analysis software (https://geneglobe.qiagen.com).

Chromatin immunoprecipitation was performed to assess MDH2 binding to the CTR2 promoter. HepG2 cells were cross-linked with 1% formaldehyde and quenched with glycine. After lysis, chromatin was fragmented by sonication to 200-500 bp. Immunoprecipitation was carried out overnight at 4°C using anti-MDH2 antibody or control IgG, followed by incubation with protein A/G magnetic beads. After washing, cross-links were reversed and DNA was purified. Precipitated DNA was analyzed by qPCR using CTR2 promoter-specific primers (Supplementary Table 1). Enrichment was normalized to input DNA and expressed as fold change relative to IgG control.

Microscale Thermophoresis (MST) Binding Analysis

Purified His-MDH2 was fluorescently labeled with the Monolith NT Protein Labeling Kit RED (NanoTemper #MO-L018) following Ni-NTA affinity chromatography. A 5′-Cy5-labeled promoter DNA fragment was incubated with serially diluted labeled protein (0.1 nM–10 μM) in binding buffer (50 mM Tris-HCl pH 7.4, 150 mM NaCl, 0.05% Tween-20) for 30 min. Binding affinities were quantified via MST using a Monolith NT.115 instrument (NanoTemper). Dissociation constants (*Kd*) were derived from nonlinear regression analysis (MO. Control software). Technical support was provided by Zoon Biotechnology (Nanjing, China).

Dual-Luciferase Reporter Assay

The promoter sequence from pAbAi-Bait was cloned into the pGL3-basic vector (Addgene #212936) using restriction enzyme-based ligation. HEK293T cells were co-transfected with the

pGL3-promoter construct, pcDNA3.1-MDH2, and pRL-TK normalization plasmid (Beyotime #D2760) using standard methods. Cells were lysed 48 h post-transfection, and dual luciferase activity was quantified with the Dual-Luciferase® Reporter Assay System (Promega #E1910), normalizing firefly luminescence to Renilla signals per manufacturer protocol.

Acetylomics

Mouse liver tissues from three biological replicates per group (n = 3 mice/group) were homogenized in RIPA lysis buffer. Proteins (2 mg per sample) were reduced with 5 mM dithiothreitol (37 °C, 30 min), alkylated with 15 mM iodoacetamide, and digested overnight with trypsin (enzyme-to-protein ratio 1:50, w/w) at 37 °C. Acetylated peptides were enriched using anti-acetyl-lysine antibody-conjugated magnetic beads (PTM-104, PTM Bio) according to manufacturer's protocol, then desalted on tC18 Sep-Pak cartridges (Waters, #WAT05496). Peptides were separated on an EASY-nLC 1200 system (Thermo) with a 90 min gradient (5–35% acetonitrile in 0.1% formic acid) at 300 nL/min, and analyzed on a Q Exactive HF-X mass spectrometer (Thermo). Full MS scans (350–1,600 m/z) were acquired at 60,000 resolution (200 m/z), followed by data-dependent HCD fragmentation (NCE 28) of the top 15 precursors at 15,000 resolution 68. Dynamic exclusion was set to 20 s. Raw data were processed in MaxQuant (v2.4.2.0) against the UniProt *Mus musculus* database (2023-10). Search parameters: trypsin/P with up to two missed cleavages; fixed modification: carbamidomethyl (C); variable modifications: acetyl (K) and oxidation (M). Precursor mass tolerance: 4.5 ppm; fragment ion tolerance: 20 ppm. Peptide and protein FDR were set to < 1% (target-decoy approach). Acetylated sites required a localization probability > 0.75 (PTM score). Label-free quantification used MaxLFQ with minimum two ratio counts. Differentially acetylated sites were defined as $|\log2(\text{ratio})| \geq 1.3$ and Benjamini-Hochberg adjusted $P < 0.05$ (two-sided t-test). Acetylome profiling was performed by PTM Bio (Hangzhou, China).

Energy metabolomics analysis

Liver tissue (n = 5 mice/grou) was homogenized in ice-cold methanol/acetonitrile/water (2:2:1, v/v/v) and vortexed for 30 s at 4 °C. Following centrifugation, supernatants were evaporated under N_2 and reconstituted in 10 mM ammonium acetate buffer (pH 9.0) containing 80% acetonitrile. Metabolites were separated at 40 °C on a SeQuant ZIC pHILIC column (150 × 2.1 mm, 5 μm, Merck) using a Vanquish Horizon UHPLC system (Thermo). Mobile phases were (A) 20 mM ammonium carbonate (pH 9.2) and (B) acetonitrile; a linear gradient from 85% to 20% B was applied over 16 min at 0.2 mL min^{-1}. Mass spectrometry was carried out on a Q Exactive HF X (Thermo) in polarity switching full scan mode (m/z 70–900, resolution 60,000 at m/z 200, AGC target 3×10^6). Raw data were processed with ProteoWizard (v. 3.0). Absolute quantification of tricarboxylic acid cycle and glycolysis intermediates was performed separately by LC MS/MS (AB Sciex 6500+, MRM mode) at Shanghai Applied Protein Technology Co., Ltd. (Shanghai, China) using external calibration curves. Metabolite levels were normalized to total ion current. Partial least squares discriminant analysis (PLS DA; VIP > 1) with a two-sided t test and Benjamini–Hochberg correction ($P < 0.05$) and KEGG pathway enrichment analysis were conducted using MetaboAnalyst 5.0.

Statistical analysis

The data represented was mean ± SEM. Statistical analyses were performed with Graphpad Prism 5.0 (GraphPad software, La Jolla, CA, USA). Sample sizes were not determined a priori by power calculations. Two-group comparisons employed two-tailed Student's t-tests, while multi-group comparisons used one-way ANOVA. Survival data were analyzed via Mantel-Cox log-rank test. Statistical significance was defined as $P < 0.05$.

Data availability

The high-throughput sequencing data generated in this study have been deposited in the Genome Sequence Archive at the National Genomics Data Center, China National Center for Bioinformation, under the following accession codes: RNA-seq (CRA016105), PacBio (CRA025000), acetylomics (OMIX009962), and energy metabolomics (OMIX009912). All relevant materials generated in this study are available from the corresponding author upon reasonable request. Source data are provided with this paper.

References

1. Pennington, H. *Escherichia coli* O157. *Lancet* **376**, 1428–1435 (2010).
2. Vihta, K.-D. et al. Trends over time in *Escherichia coli* bloodstream infections, urinary tract infections, and antibiotic susceptibilities in Oxfordshire, UK, 1998–2016: a study of electronic health records. *Lancet Infect. Dis.* **18**, 1138–1149 (2018).
3. Song, J. et al. Risk factors for *Escherichia coli* bacteraemia: a population-based case-control study. *Lancet* **390**, S85 (2017).
4. Newton, K., Dixit, V. M. & Kayagaki, N. Dying cells fan the flames of inflammation. *Science* **374**, 1076–1080 (2021).
5. Jorgensen, I., Rayamajhi, M. & Miao, E. A. Programmed cell death as a defence against infection. *Nat. Rev. Immunol*. **17**, 151–164 (2017).
6. Croxen, M. A. & Finlay, B. B. Molecular mechanisms of *Escherichia coli* pathogenicity. *Nat. Rev. Microbiol.* **8**, 26–38 (2010).
7. Wolschendorf, F. et al. Copper resistance is essential for virulence of Mycobacterium tuberculosis. *Proc. Natl Acad. Sci. USA* **108**, 1621–1626 (2011).
8. Lu, J. et al. Copper regulates the host innate immune response against bacterial infection via activation of ALPK1 kinase. *Proc. Natl Acad. Sci. USA* **121**, e2311630121 (2024).
9. Murdoch, C. C. & Skaar, E. P. Nutritional immunity: the battle for nutrient metals at the host–pathogen interface. *Nat. Rev. Microbiol.* **20**, 657–670 (2022).
10. Tsvetkov, P. et al. Copper induces cell death by targeting lipoylated TCA cycle proteins. *Science* **375**, 1254–1261 (2022).
11. Lewis, A. C. et al. Inhibition of heme biosynthesis triggers cuproptosis in acute myeloid leukemia. *Cell* **189**, 215–232.e24 (2026).
12. Kim, B.-E., Nevitt, T. & Thiele, D. J. Mechanisms for copper acquisition, distribution and regulation. *Nat. Chem. Biol.* **4**, 176–185 (2008).
13. Öhrvik, H. et al. Ctr2 regulates biogenesis of a cleaved form of mammalian Ctr1 metal transporter lacking the copper- and cisplatin-binding ecto-domain. *Proc. Natl Acad. Sci. USA*

110, E4279–E4288 (2013).
14. Paul, R. et al. Leishmania major-induced alteration of host cellular and systemic copper homeostasis drives the fate of infection. *Commun. Biol.* **7**, 1226 (2024).
15. Aryal, B. et al. Metal-induced oxidative stress and human plasma protein oxidation after SARS-CoV-2 infection. *Sci. Rep.* **13**, 2441 (2023).
16. Achard, M. E. S. et al. Copper redistribution in murine macrophages in response to Salmonella infection. *Biochem. J.* **444**, 51–57 (2012).
17. White, C., Lee, J., Kambe, T., Fritsche, K. & Petris, M. J. A role for the ATP7A copper-transporting ATPase in macrophage bactericidal activity. *J. Biol. Chem.* **284**, 33949–33956 (2009).
18. Li, S.-R., Bu, L.-L. & Cai, L. Cuproptosis: lipoylated TCA cycle proteins-mediated novel cell death pathway. *Signal Transduct. Target. Ther.* **7**, 158 (2022).
19. Lei, G. et al. Radiotherapy promotes cuproptosis and synergizes with cuproptosis inducers to overcome tumor radioresistance. *Cancer Cell* **43**, 1076–1092.e5 (2025).
20. Xie, J., Yang, Y., Gao, Y. & He, J. Cuproptosis: mechanisms and links with cancers. *Mol. Cancer* **22**, 46 (2023).
21. Tao, T. Y. & Gitlin, J. D. Hepatic copper metabolism: insights from genetic disease. *Hepatology* **37**, 1241–1247 (2003).
22. Bertinato, J., Swist, E., Plouffe, L. J., Brooks, S. P. J. & L'Abbé, M. R. Ctr2 is partially localized to the plasma membrane and stimulates copper uptake in COS-7 cells. *Biochem. J.* **409**, 731–740 (2008).
23. Zhang, X. et al. Disruption of NF-κB-mediated copper homeostasis sensitizes breast cancer to cuproptosis. *Adv. Sci.* **12**, e06201 (2025).
24. Dixon, S. J. et al. Ferroptosis: an iron-dependent form of nonapoptotic cell death. *Cell* **149**, 1060–1072 (2012).
25. Chen, X. et al. Pyroptosis is driven by non-selective gasdermin-D pore and its morphology is different from MLKL channel-mediated necroptosis. *Cell Res.* **26**, 1007–1020 (2016).
26. Hill, S. M., Phillips, A. D. & Walker-Smith, J. A. Enteropathogenic *Escherichia coli* and life-threatening chronic diarrhoea. *Gut* **32**, 154–158 (1991).
27. Drummond, R. A. et al. Long-term antibiotic exposure promotes mortality after systemic fungal infection by driving lymphocyte dysfunction and systemic escape of commensal bacteria. *Cell Host Microbe* **30**, 1020–1033.e6 (2022).
28. Schmidt, T. S. B. et al. Drivers and determinants of strain dynamics following fecal microbiota transplantation. *Nat. Med.* **28**, 1902–1912 (2022).
29. Wu, W.-L. et al. Microbiota regulate social behaviour via stress response neurons in the brain. *Nature* **595**, 409–414 (2021).
30. Clairfeuille, T. et al. Structure of the essential inner membrane lipopolysaccharide–PbgA complex. *Nature* **584**, 479–483 (2020).
31. Liu, X. et al. The existence of a nonclassical TCA cycle in the nucleus that wires the metabolic-epigenetic circuitry. *Signal Transduct. Target. Ther.* **6**, 375 (2021).
32. Cao, X. et al. Acetylation promotes TyrRS nuclear translocation to prevent oxidative damage.

Proc. Natl Acad. Sci. USA **114**, 687–692 (2017).
33. Wang, W. et al. P300/HDAC1 regulates the acetylation/deacetylation and autophagic activities of LC3/Atg8–PE ubiquitin-like system. *Cell Death Discov.* **7**, 128 (2021).
34. Narita, T., Weinert, B. T. & Choudhary, C. Functions and mechanisms of non-histone protein acetylation. *Nat. Rev. Mol. Cell Biol.* **20**, 156–174 (2019).
35. Wang, Z. et al. Genome-wide mapping of HATs and HDACs reveals distinct functions in active and inactive genes. *Cell* **138**, 1019–1031 (2009).
36. Lasko, L. M. et al. Discovery of a selective catalytic p300/CBP inhibitor that targets lineage-specific tumours. *Nature* **550**, 128–132 (2017).
37. Chow, J. C., Young, D. W., Golenbock, D. T., Christ, W. J. & Gusovsky, F. Toll-like receptor-4 mediates lipopolysaccharide-induced signal transduction. *J. Biol. Chem.* **274**, 10689–10692 (1999).
38. Gómez, H., Kellum, J. A. & Ronco, C. Metabolic reprogramming and tolerance during sepsis-induced AKI. *Nat. Rev. Nephrol.* **13**, 143–151 (2017).
39. Biram, A. et al. Bacterial infection disrupts established germinal center reactions through monocyte recruitment and impaired metabolic adaptation. *Immunity* **55**, 442–454.e8 (2022).
40. Solier, S. et al. A druggable copper-signalling pathway that drives inflammation. *Nature* **617**, 386–394 (2023).
41. Zhao, S. et al. Regulation of cellular metabolism by protein lysine acetylation. *Science* **327**, 1000–1004 (2010).
42. Lee, J. V. et al. Akt-dependent metabolic reprogramming regulates tumor cell histone acetylation. *Cell Metab.* **20**, 306–319 (2014).
43. Corbet, C. et al. Acidosis drives the reprogramming of fatty acid metabolism in cancer cells through changes in mitochondrial and histone acetylation. *Cell Metab.* **24**, 311–323 (2016).
44. Persichini, T. et al. Copper activates the NF-κB pathway in vivo. *Antioxid. Redox Signal.* **8**, 1897–1904 (2006).
45. Li, H. et al. Copper induces hepatic inflammatory responses by activation of MAPKs and NF-κB signalling pathways in the mouse. *Ecotoxicol. Environ. Saf.* **201**, 110806 (2020).
46. Liao, Y. et al. Inflammation mobilizes copper metabolism to promote colon tumorigenesis via an IL-17–STEAP4–XIAP axis. *Nat. Commun.* **11**, 900 (2020).
47. Wei, H., Frei, B., Beckman, J. S. & Zhang, W. Copper chelation by tetrathiomolybdate inhibits lipopolysaccharide-induced inflammatory responses in vivo. *Am. J. Physiol. Heart Circ. Physiol.* **301**, H712–H720 (2011).
48. Pan, Q., Bao, L. W. & Merajver, S. D. Tetrathiomolybdate inhibits angiogenesis and metastasis through suppression of the NFκB signaling cascade. *Mol. Cancer Res.* **1**, 701–706 (2003).
49. Kittredge, P. & Deane, R. S. Copper as a bacteriostatic agent. *Chest* **60**, 111–112 (1971).
50. Jasinska, W. et al. Non-consecutive enzyme interactions within TCA cycle supramolecular assembly regulate carbon-nitrogen metabolism. *Nat. Commun.* **15**, 5285 (2024).
51. Li, W. et al. Nuclear localization of mitochondrial TCA cycle enzymes modulates pluripotency via histone acetylation. *Nat. Commun.* **13**, 7414 (2022).

52. Srivastava, S. et al. Nuclear translocation of mitochondrial dehydrogenases as an adaptive cardioprotective mechanism. *Nat. Commun.* **14**, 4360 (2023).
53. Zheng, L., Roeder, R. G. & Luo, Y. S phase activation of the histone H2B promoter by OCA-S, a coactivator complex that contains GAPDH as a key component. *Cell* **114**, 255–266 (2003).
54. Kozhevnikova, E. N. et al. Metabolic enzyme IMPDH is also a transcription factor regulated by cellular state. *Mol. Cell* **47**, 133–139 (2012).
55. Chen, Y.-H. et al. MDH2 is an RNA binding protein involved in downregulation of sodium channel Scn1a expression under seizure condition. *Biochim. Biophys. Acta Mol. Basis Dis.* **1863**, 1492–1499 (2017).
56. Praharaj, M. et al. Metabolic reprogramming of tumor-associated macrophages using glutamine antagonist JHU083 drives tumor immunity in myeloid-rich prostate and bladder cancers. *Cancer Immunol. Res.* **12**, 854–875 (2024).
57. Breous, E., Somanathan, S., Bell, P. & Wilson, J. M. Inflammation promotes the loss of adeno-associated virus-mediated transgene expression in mouse liver. *Gastroenterology* **141**, 348–357.e3 (2011).
58. Mederacke, I., Dapito, D. H., Affò, S., Uchinami, H. & Schwabe, R. F. High-yield and high-purity isolation of hepatic stellate cells from normal and fibrotic mouse livers. *Nat. Protoc.* **10**, 305–315 (2015).
59. Mederacke, I. et al. The purinergic P2Y14 receptor links hepatocyte death to hepatic stellate cell activation and fibrogenesis in the liver. *Sci. Transl. Med.* **14**, eabe5795 (2022).
60. Grochowska, M. M., Bonifati, V. & Mandemakers, W. CRISPR/Cas9-mediated LRP10 knockout in HuTu-80 and HEK 293T cell lines. *Bio Protoc.* **12**, e4521 (2022).
61. Mandal, P. et al. Caspase-8 collaborates with caspase-11 to drive tissue damage and execution of endotoxic shock. *Immunity* **49**, 42–55.e6 (2018).
62. Li, L. et al. Gut microbiota from colorectal cancer patients enhances the progression of intestinal adenoma in $Apc^{min/+}$ mice. *EBioMedicine* **48**, 301–315 (2019).
63. Holmberg, S. M. et al. The gut commensal Blautia maintains colonic mucus function under low-fiber consumption through secretion of short-chain fatty acids. *Nat. Commun.* **15**, 3502 (2024).
64. Zhang, H. et al. TMEM173 drives lethal coagulation in sepsis. *Cell Host Microbe* **27**, 556–570.e6 (2020).
65. Hao, H. et al. Farnesoid X receptor regulation of the NLRP3 inflammasome underlies cholestasis-associated sepsis. *Cell Metab.* **25**, 856–867.e5 (2017).
66. Zhai, M. et al. Melatonin ameliorates myocardial ischemia reperfusion injury through SIRT3-dependent regulation of oxidative stress and apoptosis. *J. Pineal Res.* **63**, e12419 (2017).
67. Wang, X., Spandidos, A., Wang, H. & Seed, B. PrimerBank: a PCR primer database for quantitative gene expression analysis, 2012 update. *Nucleic Acids Res.* **40**, D1144–D1149 (2012).
68. Rhoads, T. W. et al. Caloric restriction engages hepatic RNA processing mechanisms in rhesus monkeys. *Cell Metab.* **27**, 677–688.e5 (2018).

Acknowledgments

We extend our heartfelt gratitude to all contributors involved in this project. Special thanks are owed to Researcher Guolan Ma and Researcher Cong Li from the Kunming Institute of Zoology, Chinese Academy of Sciences, for their expertise in flow cytometry cell sorting and confocal microscopy imaging. Additionally, we sincerely thank Ms. Hongxu Yao from Yunnan Agricultural University for her invaluable contributions to data analysis and organization. We thank LetPub (www.letpub.com.cn) for linguistic assistance and pre-submission expert review.

Funding

This work was supported by the National Natural Science Foundation of China (Approval No. 32460868， 31960692 and 31660704), the Primate Laboratory Animal Biological Sample Resource Construction Project (Approval No. 2022YFF0710902), He Zhengming Laboratory Animal Expert Workstation of Yunnan (Kunming) (Approval No. YSZJGZZ-2022063) and He Zhengming of Yunnan Province Expert Workstation (Approval No. 202305AF150160) Project fund support for this study.

Author contributions

H.W and H.G designed all experiments. H.W performed most experiments. H.W wrote the manuscript and translated it. H.G, L.B.L and Y.L.Y ensuring that data and andmaterials comply with transparency and reproducibility standards of the field and journal. J.S.Z and J.L.X assisted with, and provided conceptual advice for, multiple experiments. P.X assisted with multiple experiments. M.Z and R.Z assisted with immunoblotting experiments. J.G Z, T.L.P, and J.S assisted with microscopy image acquisition and analysis. Y.Li assisted with the bioinformatic analysis. J.Z.M provided conceptual advice for ABX mouse experiments. L.B.L and Y.L.Y provided mice and conceptual advice for FMT mouse experiments. L.P.C translation of the manuscript

Competing interests

The authors declare that they have no competing interests.

Figure legends

Fig. 1. *E. coli* infection induces cuproptosis. a Hepatic copper content post-infection was quantified by ICP-MS (n = 5 mice per group). **b** Dynamic mRNA levels of *FDX1* in livers were analyzed by qRT-PCR (n = 4 mice per group). **c** IHC analysis of FDX1 expression in livers 18 h post-infection. Arrows indicate positive staining (scale bars: 100 μm). **d** Hierarchical clustering of differentially expressed genes (DEGs) in infected livers. **e** Western blot analysis was performed to assess DLAT oligomerization, lipoylated proteins (lip-DLAT/DLST), iron–sulfur cluster proteins, TOMM20 (marker of mitochondrial abundance), and HSP70 in liver tissue collected 18 h post-infection. **f** Infection model schematic: Cells (HepG2, HeLa, A549, Vero, 293T, IPEC-j2) treated with *E. coli* (5 min) followed by 5 μM $CuCl_2$ co-treatment. **g** to **i** After the designated treatment for 5 hours, Phase-contrast microscopy revealed bubble-like death morphology in cells, scale bars: 200 μm (**g**), while CCK-8 (**h**) and LDH assays (**i**) quantified viability/cytotoxicity (n = 5 independent experiments). **j** Intracellular copper levels in HepG2 cells were measured using ICP-MS at 5 hours post-infection (n = 4 independent experiments). **k** qRT-PCR analysis of *FDX1* mRNA levels after infection (left) or *E. coli*, $CuCl_2$ co-treatment (right) (n = 6 independent experiments). **l** and **m** DLAT oligomerization was assessed by western blot (**l**) and confocal imaging (**m**) after 2.5 hours treatment in HepG2 cells (DLAT-green, MitoTracker-red, DAPI-blue, arrows-oligomeric DLAT, scale bars: 2 μm). **n** Pretreatment with cells death pathway inhibitors (TTM, Z-VAD-FMK, Fer-1, Necr-1, 3-MA) prior to *E. coli*/$CuCl_2$ co-treatment (5 h after infection, observed using phase-contrast microscopy- representative images, scale bars: 200 μm). **o** Western blot analysis of markers for multiple programmed cell death pathways in the presence or absence of $CuCl_2$ during infection. **p** DLAT oligomerization assessed by western blot across multiple cell lines after 5 hours of treatment. **q** Heatmap of cell viability (CCK-8 assay) in cells co-treated with *E. coli* and $CuCl_2$ by pretreatment with various inhibitors (n = 4 independent experiments). Data are presented as mean ± SEM. (Ordinary one-way ANOVA in a, b, h, i, j, and k).

Fig. 2. *E. coli* upregulates CTR2 to disrupt copper homeostasis. a Hepatic *SLC31A1/2* mRNA levels post-infection were quantified by qRT-PCR (n =8 mice per group). **b** CTR1/2 protein levels in livers 18 h post-infection. **c** Lysosomal, plasma membrane, and cytosolic fractions were isolated from cells treated with *E. coli* + $CuCl_2$ for 3 h, and CTR2 subcellular distribution was assessed by immunoblotting. **d** Morphological changes in cells (OE-CTR2) exposed to $CuCl_2$ were observed by phase-contrast microscopy- representative images, scale bars: 200 μm. **e** Intracellular copper levels in HepG2 cells (OE-CTR2) 5 h post-$CuCl_2$ treatment measured by ICP-MS (n = 4 independent experiments). **f** Western blot analysis of DLAT oligomerization in HepG2 cells supplemented with $CuCl_2$. **g** Liver-specific CTR2 overexpression model via rAAV-TBG-

mCherry-CTR2 tail-vein delivery (OE-CTR2 mouse). **h** Western blot analysis of cuproptosis markers in livers of OE-CTR2 mice after infection. **i** Copper levels in HepG2 cells post-infection (5 h) were determined by ICP-MS (n = 4 independent experiments). **j** Western blot assessment of DLAT oligomerization in CTR1/2$^{-/-}$ cells 5 h post-*E. coli*/$CuCl_2$ co-treatment. **k** Diagram illustrating the mechanism by which *E. coli* triggers cuproptosis. **l** Confocal imaging of DLAT oligomerization in cells following $CuCl_2$ exposure (DLAT-green, MitoTracker-red, DAPI-blue, scale bars = 2 μm), ES-$CuCl_2$ (1:1) served as a positive control. **m** to **o** TEM images of cells 8 h after treatment, lower panels showing higher-magnification views of the boxed regions in upper panels. Normal mitochondria (blue arrows), cristae loss/membrane damage with increased density (red arrows), autophagosome-encapsulated mitochondria (purple arrows) (scale bars = 2 μm). Quantification of damaged mitochondria shown in **n** (percentage) and **o** (count). **p** Confocal imaging of mitochondrial mass (Red, upper) and mitochondrial ROS (Red, lower) 2.5 h after treatment (Hoechst-blue, scale bars = 10 μm). **q** SEM images of cells (scale bars = 10 μm), arrows indicate bubble-like protrusions on the cell surface following cuproptosis. Data are presented as mean ± SEM. (Ordinary one-way ANOVA in a, e, i, n, and o).

Fig. 3. The morphological characteristics of Cuproptosis at different times. a SEM images of cells at various times following designated treatments (scale bars = 10 μm). Arrows indicate the blister-like protrusions on the cell surface associated with cuproptosis. **b** Confocal imaging of DLAT oligomerization in cells (OE-hCTR2) following CuCl2 exposure (DLAT-green, MitoTracker-red, DAPI-blue, scale bars = 2 μm), ES-CuCl2 (1:1) served as a positive control.

Fig. 4. The "gut-LPS-liver axis" regulation in *E. coli* induced cuproptosis. a Intestinal copper content post-infection quantified by ICP-MS (n = 6 mice per group). **b** to **d** Western blot analysis of cuproptosis markers in intestinal (**b**, **d**) and hepatic (**c**) tissues at indicated time points post-infection. **e** PacBio-based microbial diversity sequencing to evaluate species abundance in the gut after infection, visualized via LEfSe bar plots. **f** Functional prediction of the gut microbiota using PICRUSt2/KEGG. **g** ELISA measurement of LPS levels in liver (left) and serum (right) post-infection (n = 6 mice per group). **h** Schematic of the *E. coli* infection protocols in ABX and FMT mouse models: ABX mice were generated by an antibiotic cocktail, ABX mice were gavaged with fecal suspensions of infected donors to produce FMT mice, with a 3-day washout period prior to transplantation. **i** Western blot detection of DLAT oligomerization in liver: compare NC and ABX mice post- infection (upper), compare ABX and FMT mice(lower). **j** Gut histopathology by H&E staining (upper, scale bars = 50 μm, red arrows-epithelial cell death (loss of nuclei), blue arrows-villus disruption) and hepatic IL-1β expression by IHC 18 h after infection (lower, scale bars = 50 μm). **k** ELISA quantification of serum LPS of specific mice at 18 h after infection (n = 6 mice per group). **l** Confocal imaging of DLAT oligomerization in cells treated with $CuCl_2$ or $CuCl_2$/LPS for 2.5 h (DLAT-green, MitoTracker-red, DAPI-blue, scale bars = 2 μm). **m** Western blot analysis of cuproptosis markers in CTR1$^{-/-}$ and CTR2$^{-/-}$ cells treated with $CuCl_2$ alone or in combination with LPS for 5 hours. Data are presented as mean ± SEM. (Ordinary one-way ANOVA in a, g, and k).

Fig. 5. Mitochondrial MDH2 regulates CTR2 promoter activity. a Schematic diagram of genome-wide Y1H screen using the CTR2 promoter (pCTR2) as bait. **b** PCR array analysis of yeast library-enriched genes in infected livers (12 h post-infection, volcano plot: red—upregulated, blue—downregulated, two-tailed tests with correction for multiple comparisons). **c** Y1HGold[pAbAi-pCTR2] yeast transformed with pGADT7-MDH2, cultured on SD/-Leu + 200 ng/mL AbA. Serial dilutions spotted for growth validation. **d** MST assessment of binding between His-MDH2 protein and the CTR2 promoter, *Kd* = 0.62 μM. upper-binding curve, panel-*Kd* calculated. **e** Co-transfection of serial plasmids into HEK293T cells, followed 48 h later by dual-luciferase reporter assay to confirm interaction between MDH2 and the CTR2 promoter (n = 8 independent experiments). **f** ChIP–qPCR analysis of MDH2 binding to the CTR2 promoter region. **g** Confocal imaging of MDH2 localization in cells treated with $CuCl_2$ or co-treated with LPS for 2.5 h (MDH2-green, MitoTracker-red, DAPI-blue, scale bar = 2 μm). **h** IHC detection of MDH2 localization in liver, with representative regions highlighted by white boxes (scale bar = 50 μm). **i** Experimental schematic of the HepG2 or HeLa cells LPS treatment model (OE-MDH2 or $MDH2^{-/-}$ cells): cells were stimulated with LPS for 5 min, then treated with $CuCl_2$ for specified durations. **j** Western blot analysis of cuproptosis markers in OE-MDH2 cells 5 hours after $CuCl_2$ treatment. **k** After 5 hours of $CuCl_2$ treatment, the copper content in the designated treated cells was quantified by ICP-MS (n = 6 independent experiments). **l** qRT-PCR measurement of *SLC31A2* mRNA levels in designated treated cells (n = 10 independent experiments). **m** to **p** Western blot analysis of cuproptosis markers in OE-MDH2 (**m**, **n**) and $MDH2^{-/-}$ (**o**, **p**) cells treated with $CuCl_2$ alone or in combination with LPS for 5 hours. **q** Morphological changes in OE-CTR2 cells exposed to $CuCl_2$ were assessed, and representative images are shown, scale bars = 200 μm. Data are presented as mean ± SEM. (Ordinary one-way ANOVA in e, f, k, and l).

Fig. 6. Acetylation drives MDH2 nuclear translocation and metabolic reprogramming. a Global protein acetylation in HepG2 cells 5 h after treatment with $CuCl_2$ alone, $CuCl_2$ plus *E. coli*, or $CuCl_2$ plus LPS. **b** Acetylation of Myc-MDH2 in HepG2 cells under $CuCl_2$ or $CuCl_2$/LPS treatment. Myc-MDH2 was immunoprecipitated (IP) with anti-Myc, and the precipitates were analyzed using an anti-acetyl-lys antibody. Acetylation of endogenous MDH2, MDH2 acetylation was analyzed by IP with an anti-Ace-lys antibody. **c** and **d** Hepatic acetylomics 18 h after infection. Volcano plot showing differentially acetylated proteins (red-upregulated, blue-downregulated, two-tailed tests with correction for multiple comparisons). Three lysine residues of MDH2 showing significant acetylation (**c**), Mass-spectrometry data of the acetylation at MDH2-K297(**d**). **e** Mass spectrometric quantification of acetylation at distinct lysine residues of MDH2. **f** Hierarchical clustering of infection-regulated, acetylation-associated differentially expressed genes. **g** Acetylation of exogenous Myc-MDH2 in HepG2 cells treated with TSA and/or NAM. **h** Following Sirt3 knockdown or 3-TYP treatment, endogenous MDH2 acetylation was assessed by immunoprecipitation (IP). **i** GST pull-down assay using recombinant His-Sirt3 and GST-MDH2 confirmed direct interaction between MDH2 and Sirt3. **j** Confocal imaging of cells treated with 3-TYP for 6 h revealed MDH2 localization (MDH2-green, MitoTracker-red, DAPI-blue, scale bars = 2 μm). **k** Nuclear/cytoplasmic fractionation followed by western blot to assess MDH2

localization in 3-TYP treated cells (5 h). **l** Western blot analysis of endogenous MDH2 acetylation and protein content in cells following 3-TYP treatment. **m** After combined shRNA-Sirt3 and $CuCl_2$ pretreatment, the MDH2 localization and cuproptosis were detected by western blot. **n** Endogenous MDH2 acetylation and Sirt3 expression in $TLR4^{-/-}$ cells. **o** DLAT oligomerization in WT and $TLR4^{-/-}$ cells 5 h after $CuCl_2$ or $CuCl_2$/LPS treatment. **p** KEGG analysis of differentially abundant metabolites in liver post-infection identified the top 20 pathways (One-sided tests with correction for multiple comparisons). **q** Hierarchical clustering of targeted metabolomics profiling of TCA-cycle metabolites in liver. **r** Activities of TCA cycle enzymes in liver were measured colorimetrically and mapped onto the TCA cycle diagram. Data are presented as mean ± SEM. (Ordinary one-way ANOVA in e, two-tailed Student's *t*-tests in r).

Fig. 7. Inhibition of cuproptosis alleviates *E. coli*-induced liver injury. a Experimental design: WT and $CTR2^{-/-}$ mice were infected with *E. coli* and sampled at defined timepoints, with a subset pretreated with TTM. **b** Survival rates of infected mice (n = 15 mice per group). **c** Hepatic bacterial burden post-infection, scatter diagram shows all data points (n = 15 mice per group). **d** Hepatic copper content in infected mice (WT or $CTR2^{-/-}$) was measured by ICP-MS (n = 6 mice per group). **e** Western blot analysis of DLAT oligomerization in livers of mice 18 h post-infection, with or without TTM pretreatment. **f** Organ indices for the liver were normalized to assess tissue swelling (n = 5 mice per group). **g** Biochemical analysis of serum ALT (left) and AST (right) levels in mice 18 h post-infection under designated treatments (n = 5 mice per group). **h** ELISA quantification of serum IL-18 (left) and TNF-α (right) levels in mice 18 h post-infection under designated treatments (n = 5 mice per group). **i** Liver histopathology (H&E): with representative areas enlarged and highlighted by black boxes, red arrows-hepatocyte death (loss of nuclei), blue arrows-disrupted hepatic cord structure, scale bars: 50 μm. **j** Triple immunofluorescence staining of liver sections: F4/80 (macrophages, red), CD86 (M1 polarization, yellow), CD11b (neutrophils, green), and DAPI (nuclei, blue). Boxed regions show progressive magnification (scale bars: 50 μm). Data are presented as mean ± SEM. (Mantel-Cox log-rank tes in b; Ordinary one-way ANOVA in c, d, f, g, and h).

Fig. 8. A schematic mechanism model of *Escherichia coli*-induced cuproptosis. *E. col*i infection activates the gut–LPS–liver axis. Gut dysbiosis elevates circulating lipopolysaccharide (LPS). Hepatic LPS signals via TLR4–Sirt3 to acetylate mitochondrial malate dehydrogenase 2 (MDH2). Acetylated MDH2 translocates to the nucleus, binding the *SLC31A2* (CRT2) promoter to upregulate the copper transporter CTR2. Excessive copper influx causes intracellular copper overload, disrupting Fe–S cluster proteins and inducing DLAT aggregation, which triggers cuproptosis. These events, accompanied by immune infiltration and TCA cycle reprogramming, drive acute liver injury.

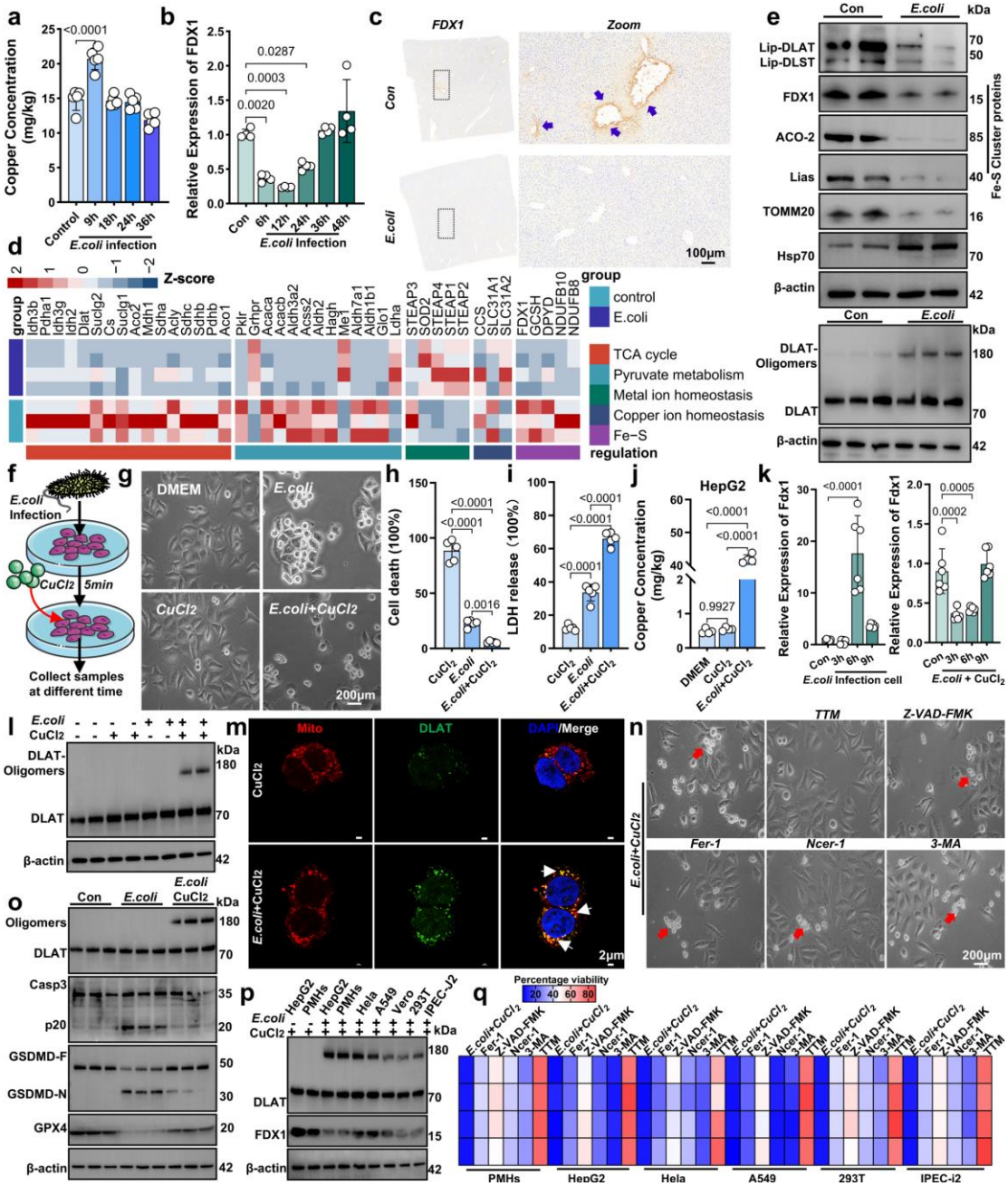
a
Copper Concentration (mg/kg)
<0.0001
Control
9h
18h
24h
36h
E.coli infection
b
Relative Expression of FDX1
0.0287
0.0003
0.0020
Con
6h
12h
24h
36h
48h
E.coli Infection
c
FDX1
Zoom
Con
E.coli
100μm
d
Z-score
group
control
E.coli
TCA cycle
Pyruvate metabolism
Metal ion homeostasis
Copper ion homeostasis
Fe−S
regulation
e
Con
E.coli
kDa
Lip-DLAT
Lip-DLST
FDX1
ACO-2
Lias
TOMM20
Hsp70
β-actin
Fe-S Cluster proteins
DLAT-Oligomers
DLAT
f
E.coli Infection
CuCl2 5min
Collect samples at different time
g
DMEM
E.coli
CuCl2
E.coli+CuCl2
200μm
h
Cell death (100%)
<0.0001
0.0016
i
LDH release (100%)
j
HepG2
Copper Concentration (mg/kg)
0.9927
k
Relative Expression of Fdx1
0.0005
0.0002
E.coli Infection cell
E.coli + CuCl2
l
DLAT-Oligomers
DLAT
β-actin
m
Mito
DLAT
DAPI/Merge
CuCl2
E.coli+CuCl2
2μm
n
TTM
Z-VAD-FMK
Fer-1
Ncer-1
3-MA
E.coli+CuCl2
200μm
o
Oligomers
DLAT
Casp3
p20
GSDMD-F
GSDMD-N
GPX4
β-actin
p
HepG2
PMHs
Hela
A549
Vero
293T
IPEC-J2
DLAT
FDX1
β-actin
q
Percentage viability
PMHs
HepG2
Hela
A549
293T
IPEC-i2

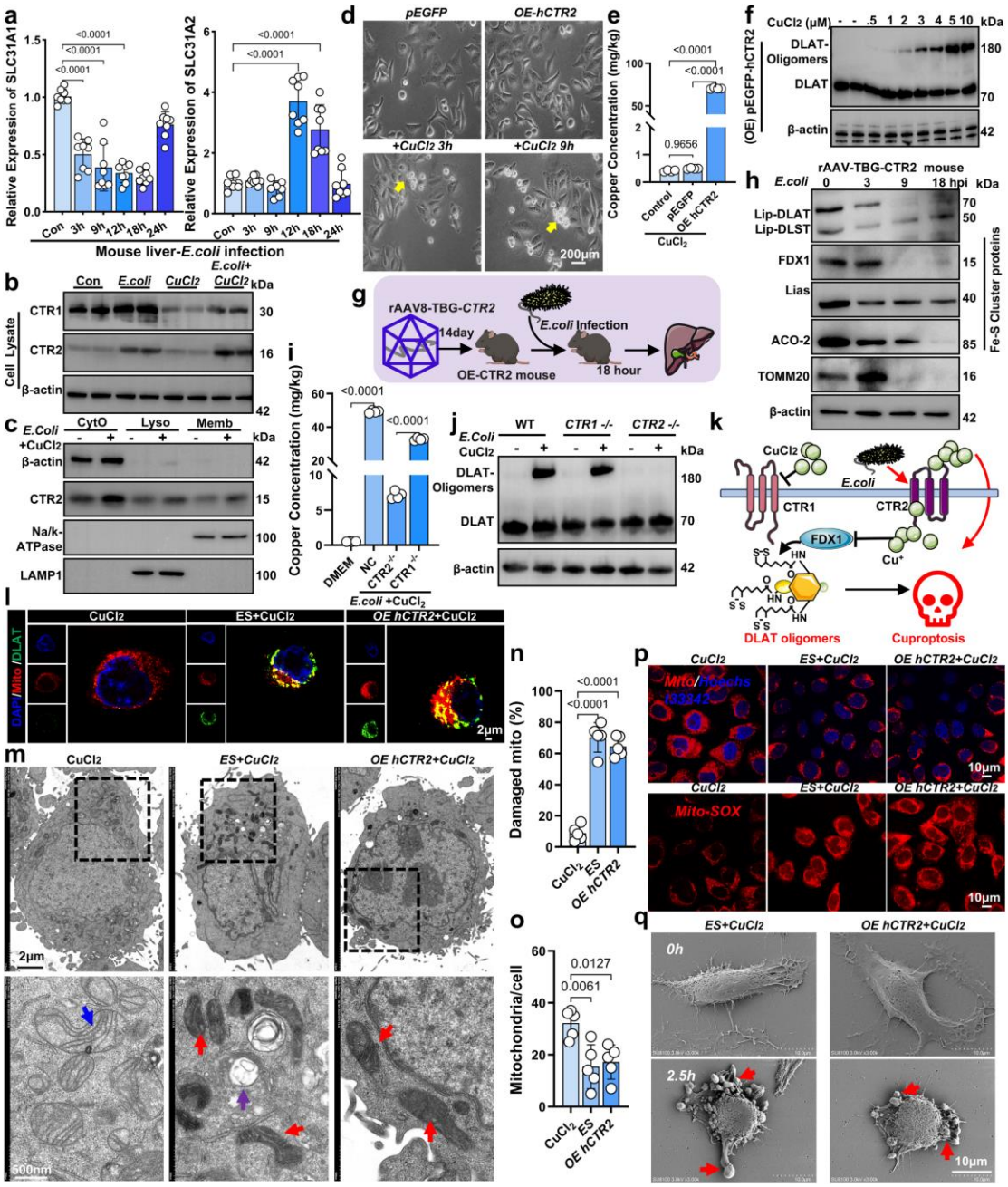
a
Relative Expression of SLC31A1
Relative Expression of SLC31A2
Con 3h 9h 12h 18h 24h
Mouse liver-E.coli infection
b
Con E.coli CuCl2 E.coli+CuCl2 kDa
Cell Lysate
CTR1
CTR2
β-actin
c
E.Coli +CuCl2
CytO Lyso Memb
β-actin
CTR2
Na/k-ATPase
LAMP1
d
pEGFP
OE-hCTR2
+CuCl2 3h
+CuCl2 9h
200μm
e
Copper Concentration (mg/kg)
0.9656
Control pEGFP OE hCTR2
CuCl2
f
CuCl2 (μM) - - .5 1 2 3 4 5 10 kDa
(OE) pEGFP-hCTR2
DLAT-Oligomers
DLAT
β-actin
g
rAAV8-TBG-CTR2
14day
E.coli Infection
OE-CTR2 mouse
18 hour
h
rAAV-TBG-CTR2 mouse
E.coli 0 3 9 18 hpi kDa
Lip-DLAT
Lip-DLST
FDX1
Lias
ACO-2
TOMM20
β-actin
Fe-S Cluster proteins
i
Copper Concentration (mg/kg)
DMEM NC CTR2-/- CTR1-/-
E.coli +CuCl2
j
E.Coli CuCl2
WT CTR1 -/- CTR2 -/-
DLAT-Oligomers
DLAT
β-actin
k
CuCl2
E.coli
CTR1
CTR2
FDX1
Cu+
DLAT oligomers
Cuproptosis
l
CuCl2
ES+CuCl2
OE hCTR2+CuCl2
DAPI/Mito/DLAT
2μm
m
CuCl2
ES+CuCl2
OE hCTR2+CuCl2
2μm
500nm
n
Damaged mito (%)
CuCl2 ES OE hCTR2
o
Mitochondria/cell
0.0127
0.0061
CuCl2 ES OE hCTR2
p
CuCl2
ES+CuCl2
OE hCTR2+CuCl2
Mito/Hoechs 33342
Mito-SOX
10μm
q
ES+CuCl2
OE hCTR2+CuCl2
0h
2.5h
10μm

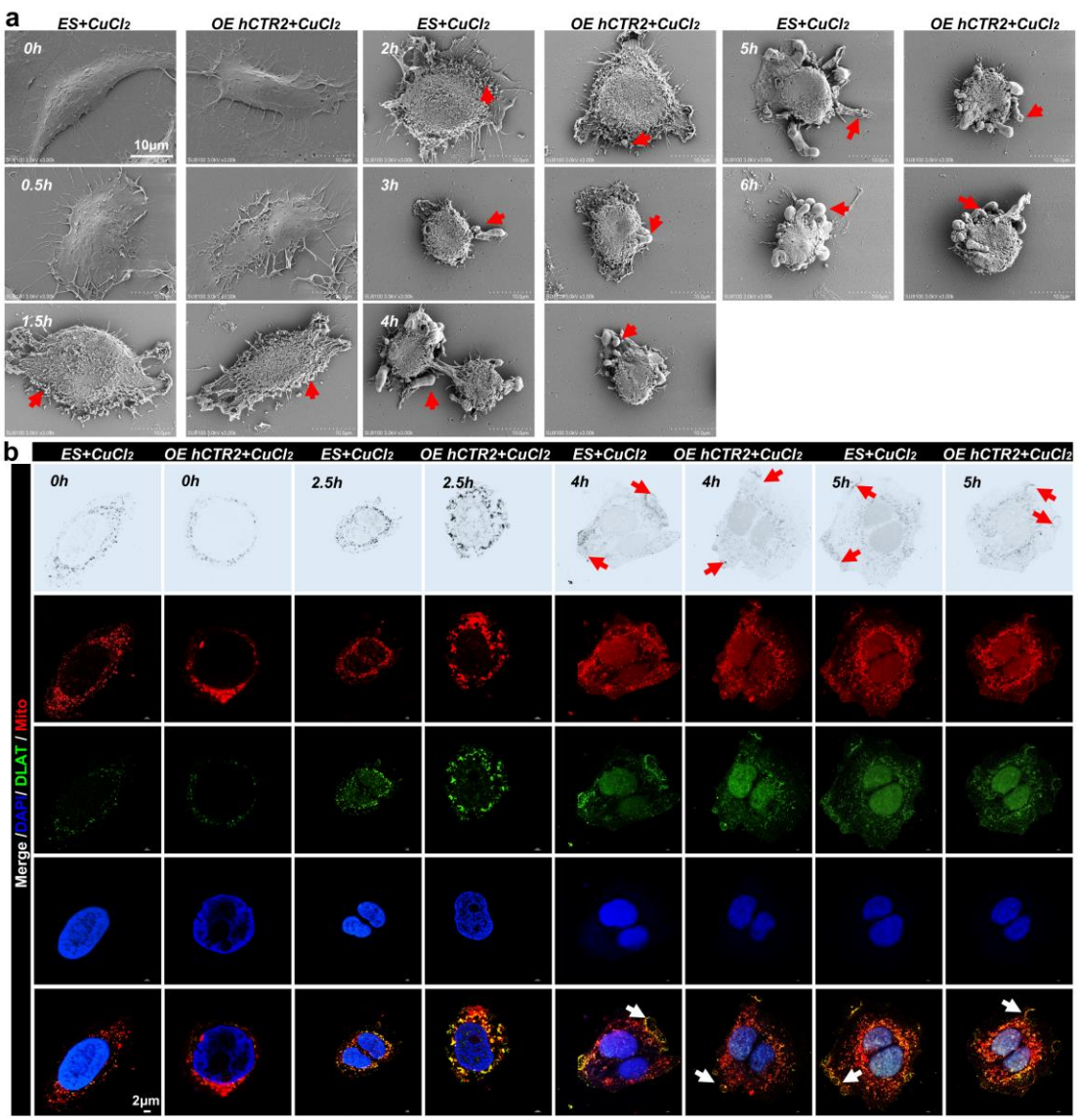
a
ES+CuCl2
OE hCTR2+CuCl2
ES+CuCl2
OE hCTR2+CuCl2
ES+CuCl2
OE hCTR2+CuCl2
0h
10μm
2h
5h
0.5h
3h
6h
1.5h
4h
b
ES+CuCl2
OE hCTR2+CuCl2
ES+CuCl2
OE hCTR2+CuCl2
ES+CuCl2
OE hCTR2+CuCl2
ES+CuCl2
OE hCTR2+CuCl2
0h
0h
2.5h
2.5h
4h
4h
5h
5h
Merge /DAPI/ DLAT / Mito
2μm

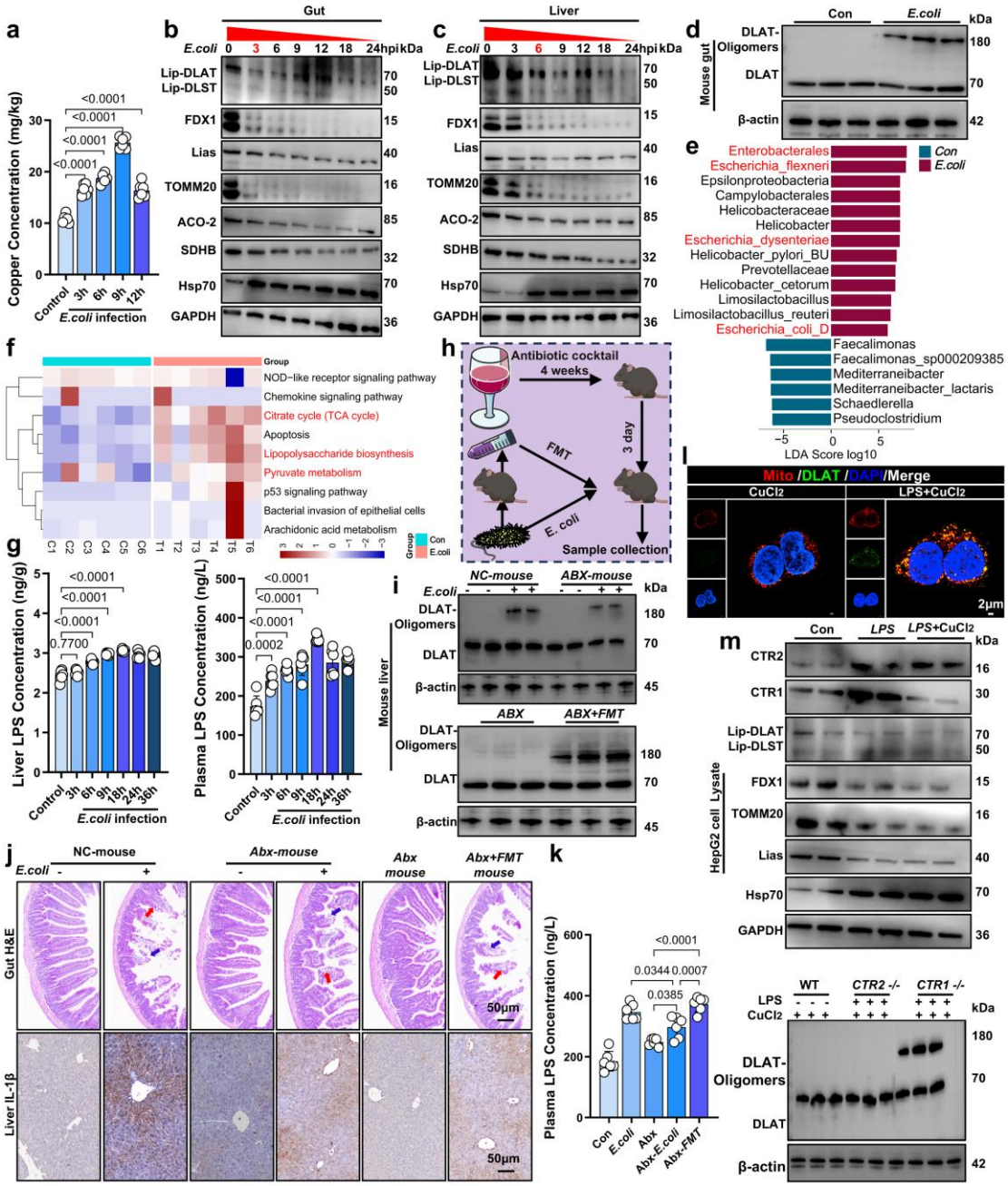
a
Copper Concentration (mg/kg)
<0.0001
Control
3h
6h
9h
12h
E.coli infection
b
Gut
E.coli
0 3 6 9 12 18 24hpi
kDa
Lip-DLAT
Lip-DLST
FDX1
Lias
TOMM20
ACO-2
SDHB
Hsp70
GAPDH
c
Liver
d
Con
E.coli
Mouse gut
DLAT-Oligomers
DLAT
β-actin
e
Enterobacterales
Escherichia_flexneri
Epsilonproteobacteria
Campylobacterales
Helicobacteraceae
Helicobacter
Escherichia_dysenteriae
Helicobacter_pylori_BU
Prevotellaceae
Helicobacter_cetorum
Limosilactobacillus
Limosilactobacillus_reuteri
Escherichia_coli_D
Faecalimonas
Faecalimonas_sp000209385
Mediterraneibacter
Mediterraneibacter_lactaris
Schaedlerella
Pseudoclostridium
LDA Score log10
f
Group
NOD−like receptor signaling pathway
Chemokine signaling pathway
Citrate cycle (TCA cycle)
Apoptosis
Lipopolysaccharide biosynthesis
Pyruvate metabolism
p53 signaling pathway
Bacterial invasion of epithelial cells
Arachidonic acid metabolism
h
Antibiotic cocktail
4 weeks
FMT
3 day
E. coli
Sample collection
l
Mito /DLAT /DAPI/Merge
CuCl2
LPS+CuCl2
2μm
g
Liver LPS Concentration (ng/g)
Plasma LPS Concentration (ng/L)
0.7700
0.0002
i
NC-mouse
ABX-mouse
ABX
ABX+FMT
Mouse liver
m
Con
LPS
LPS+CuCl2
CTR2
CTR1
HepG2 cell Lysate
j
NC-mouse
Abx-mouse
Abx mouse
Abx+FMT mouse
Gut H&E
Liver IL-1β
50μm
k
Plasma LPS Concentration (ng/L)
0.0344
0.0007
0.0385
Con
E.coli
Abx
Abx-E.coli
Abx-FMT
WT
CTR2 -/-
CTR1 -/-
LPS
CuCl2

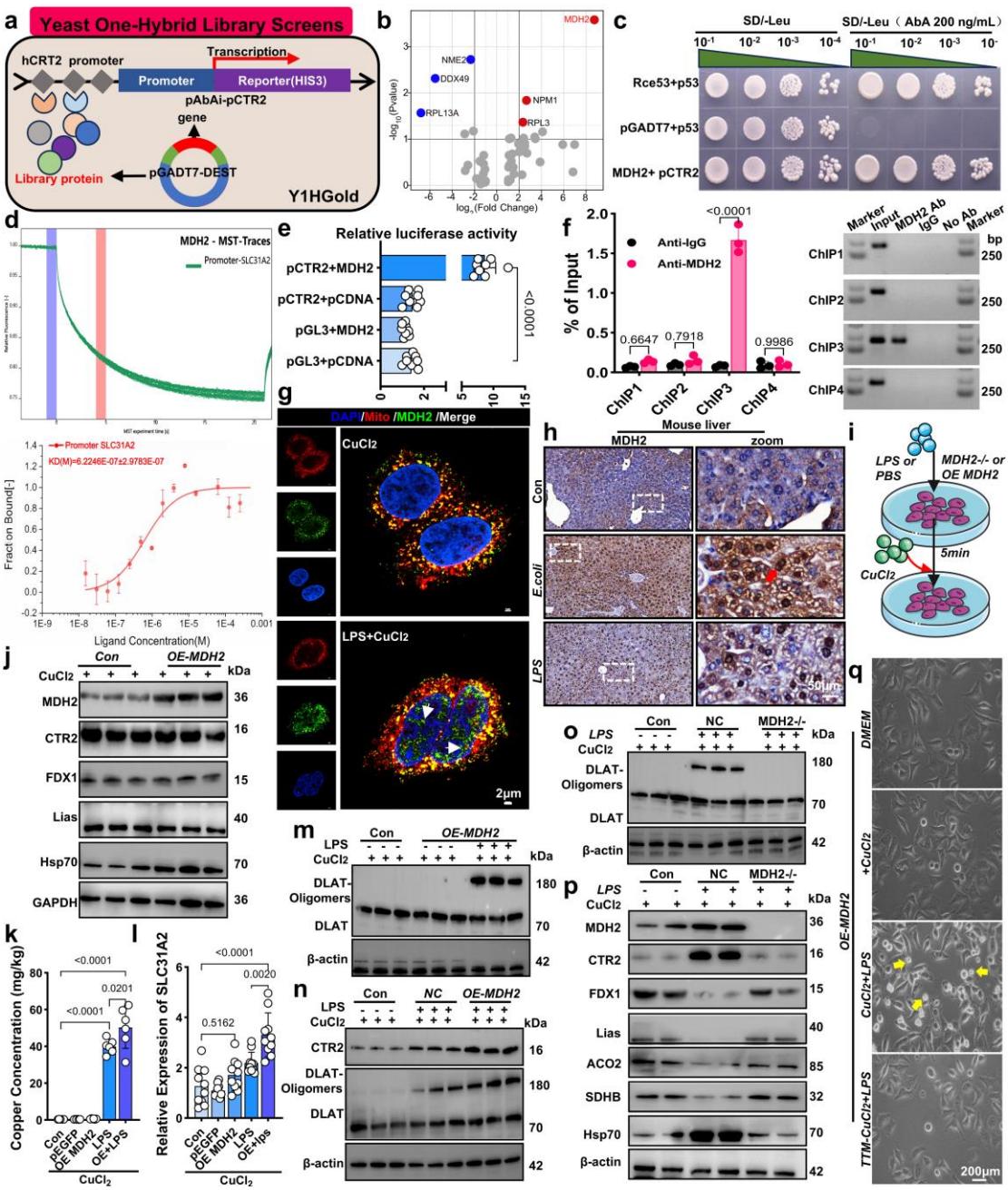
a
Yeast One-Hybrid Library Screens
hCRT2 promoter
Transcription
Promoter
Reporter(HIS3)
pAbAi-pCTR2
gene
Library protein
pGADT7-DEST
Y1HGold
b
MDH2
NME2
DDX49
NPM1
RPL13A
RPL3
-log10(Pvalue)
log2(Fold Change)
c
SD/-Leu
SD/-Leu（AbA 200 ng/mL）
Rce53+p53
pGADT7+p53
MDH2+ pCTR2
d
MDH2 - MST-Traces
Promoter-SLC31A2
Promoter SLC31A2
KD(M)=6.2246E-07±2.9783E-07
Fraction Bound[-]
Ligand Concentration(M)
e
Relative luciferase activity
pCTR2+MDH2
pCTR2+pCDNA
pGL3+MDH2
pGL3+pCDNA
<0.0001
f
Anti-IgG
Anti-MDH2
% of Input
0.6647
0.7918
<0.0001
0.9986
ChIP1
ChIP2
ChIP3
ChIP4
Marker
Input
MDH2 Ab
IgG
No Ab
Marker
bp
250
g
DAPI/Mito /MDH2 /Merge
CuCl2
LPS+CuCl2
2μm
h
Mouse liver
MDH2
zoom
Con
E.coli
LPS
50μm
i
LPS or PBS
MDH2-/- or OE MDH2
5min
CuCl2
j
Con
OE-MDH2
CuCl2
kDa
MDH2
CTR2
FDX1
Lias
Hsp70
GAPDH
36
16
15
40
70
36
k
Copper Concentration (mg/kg)
<0.0001
0.0201
<0.0001
Con
pEGFP
OE MDH2
LPS
OE+LPS
CuCl2
l
Relative Expression of SLC31A2
<0.0001
0.0020
0.5162
Con
pEGFP
OE MDH2
LPS
OE+lps
CuCl2
m
Con
OE-MDH2
LPS
CuCl2
kDa
DLAT-Oligomers
DLAT
β-actin
180
70
42
n
Con
NC
OE-MDH2
LPS
CuCl2
kDa
CTR2
DLAT-Oligomers
DLAT
β-actin
16
180
70
42
o
Con
NC
MDH2-/-
LPS
CuCl2
kDa
DLAT-Oligomers
DLAT
β-actin
180
70
42
p
Con
NC
MDH2-/-
LPS
CuCl2
kDa
MDH2
CTR2
FDX1
Lias
ACO2
SDHB
Hsp70
β-actin
36
16
15
40
85
32
70
42
q
DMEM
+CuCl2
CuCl2+LPS
TTM-CuCl2+LPS
OE-MDH2
200μm

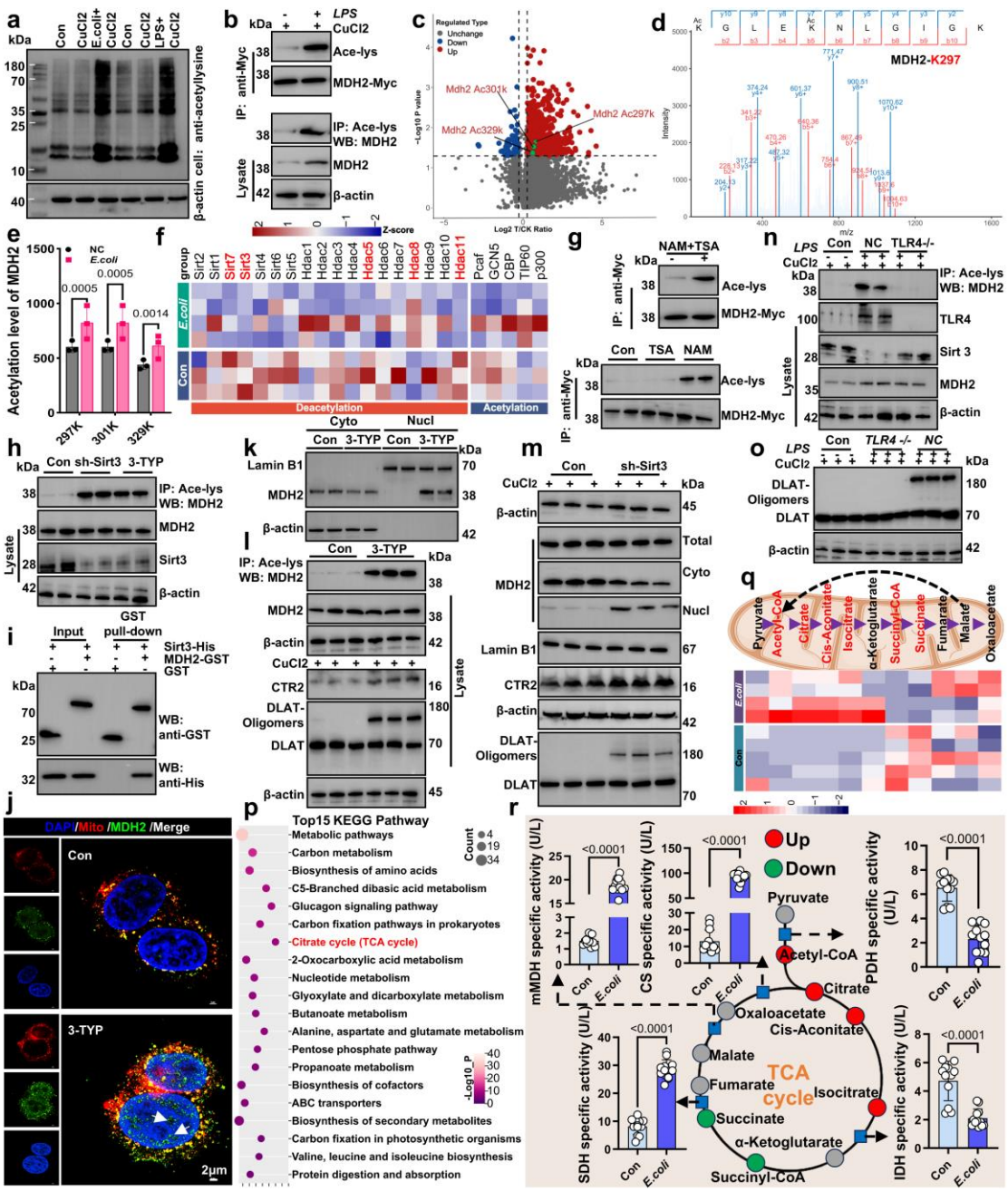
a
Con
CuCl2
E.coli+ CuCl2
Con
CuCl2 LPS+ CuCl2
kDa
180
70
35
25
10
40
β-actin cell: anti-acetyllysine
b
LPS
CuCl2
IP: anti-Myc
Ace-lys
MDH2-Myc
IP: Ace-lys WB: MDH2
Lysate
MDH2
β-actin
Z-score
c
Regulated Type
Unchange
Down
Up
Mdh2 Ac301k
Mdh2 Ac329k
Mdh2 Ac297k
-Log10 P-value
Log2 T/CK Ratio
d
MDH2-K297
Intensity
m/z
e
Acetylation level of MDH2
NC
E.coli
0.0005
0.0005
0.0014
297K
301K
329K
f
group
Sirt2
Sirt1
Sirt7
Sirt3
Sirt4
Sirt6
Sirt5
Hdac1
Hdac2
Hdac3
Hdac4
Hdac5
Hdac6
Hdac7
Hdac8
Hdac9
Hdac10
Hdac11
Pcaf
GCN5
CBP
TIP60
p300
E.coli
Con
Deacetylation
Acetylation
g
NAM+TSA
IP: anti-Myc
Ace-lys
MDH2-Myc
Con
TSA
NAM
n
LPS
CuCl2
Con
NC
TLR4-/-
IP: Ace-lys WB: MDH2
TLR4
Sirt 3
MDH2
β-actin
Lysate
h
Con
sh-Sirt3
3-TYP
IP: Ace-lys WB: MDH2
MDH2
Sirt3
β-actin
Lysate
GST
i
Input
pull-down
Sirt3-His
MDH2-GST
GST
WB: anti-GST
WB: anti-His
k
Cyto
Nucl
Con
3-TYP
Lamin B1
MDH2
β-actin
l
IP: Ace-lys WB: MDH2
CTR2
DLAT-Oligomers
DLAT
Lysate
m
sh-Sirt3
Total
Cyto
Nucl
o
TLR4 -/-
NC
DLAT-Oligomers
DLAT
q
Pyruvate
Acetyl-CoA
Citrate
Cis-Aconitate
Isocitrate
α-Ketoglutarate
Succinyl-CoA
Succinate
Fumarate
Malate
Oxaloacetate
j
DAPI/Mito /MDH2 /Merge
Con
3-TYP
2μm
p
Top15 KEGG Pathway
Count
Metabolic pathways
Carbon metabolism
Biosynthesis of amino acids
C5-Branched dibasic acid metabolism
Glucagon signaling pathway
Carbon fixation pathways in prokaryotes
Citrate cycle (TCA cycle)
2-Oxocarboxylic acid metabolism
Nucleotide metabolism
Glyoxylate and dicarboxylate metabolism
Butanoate metabolism
Alanine, aspartate and glutamate metabolism
Pentose phosphate pathway
Propanoate metabolism
Biosynthesis of cofactors
ABC transporters
Biosynthesis of secondary metabolites
Carbon fixation in photosynthetic organisms
Valine, leucine and isoleucine biosynthesis
Protein digestion and absorption
-Log10_P
r
mMDH specific activity (U/L)
CS specific activity (U/L)
PDH specific activity (U/L)
SDH specific activity (U/L)
IDH specific activity (U/L)
<0.0001
Con
E.coli
Up
Down
Pyruvate
Acetyl-CoA
Citrate
Oxaloacetate
Cis-Aconitate
Malate
Fumarate
Isocitrate
Succinate
α-Ketoglutarate
Succinyl-CoA
TCA cycle

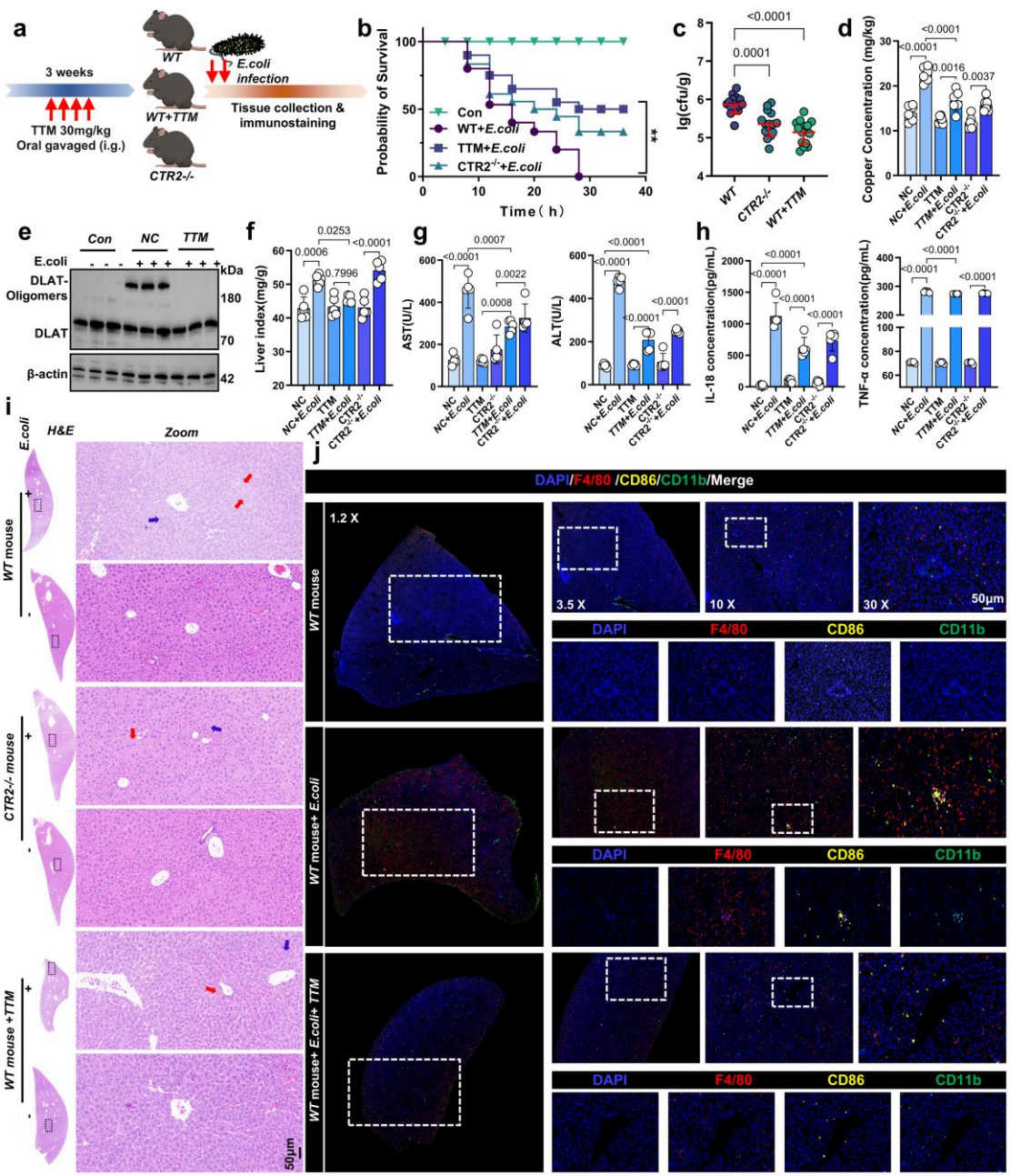
a
3 weeks
TTM 30mg/kg
Oral gavaged (i.g.)
WT
WT+TTM
CTR2-/-
E.coli infection
Tissue collection & immunostaining
b
Probability of Survival
Time（h）
Con
WT+E.coli
TTM+E.coli
CTR2-/-+E.coli
c
lg(cfu/g)
d
Copper Concentration (mg/kg)
e
Con
NC
TTM
E.coli
DLAT-Oligomers
DLAT
β-actin
kDa
f
Liver index(mg/g)
g
AST(U/L)
ALT(U/L)
h
IL-18 concentration(pg/mL)
TNF-α concentration(pg/mL)
i
H&E
Zoom
WT mouse
CTR2-/- mouse
WT mouse +TTM
50μm
j
DAPI/F4/80 /CD86/CD11b/Merge
WT mouse
WT mouse+ E.coli
WT mouse+ E.coli+ TTM
1.2 X
3.5 X
10 X
30 X
50μm
DAPI
F4/80
CD86
CD11b

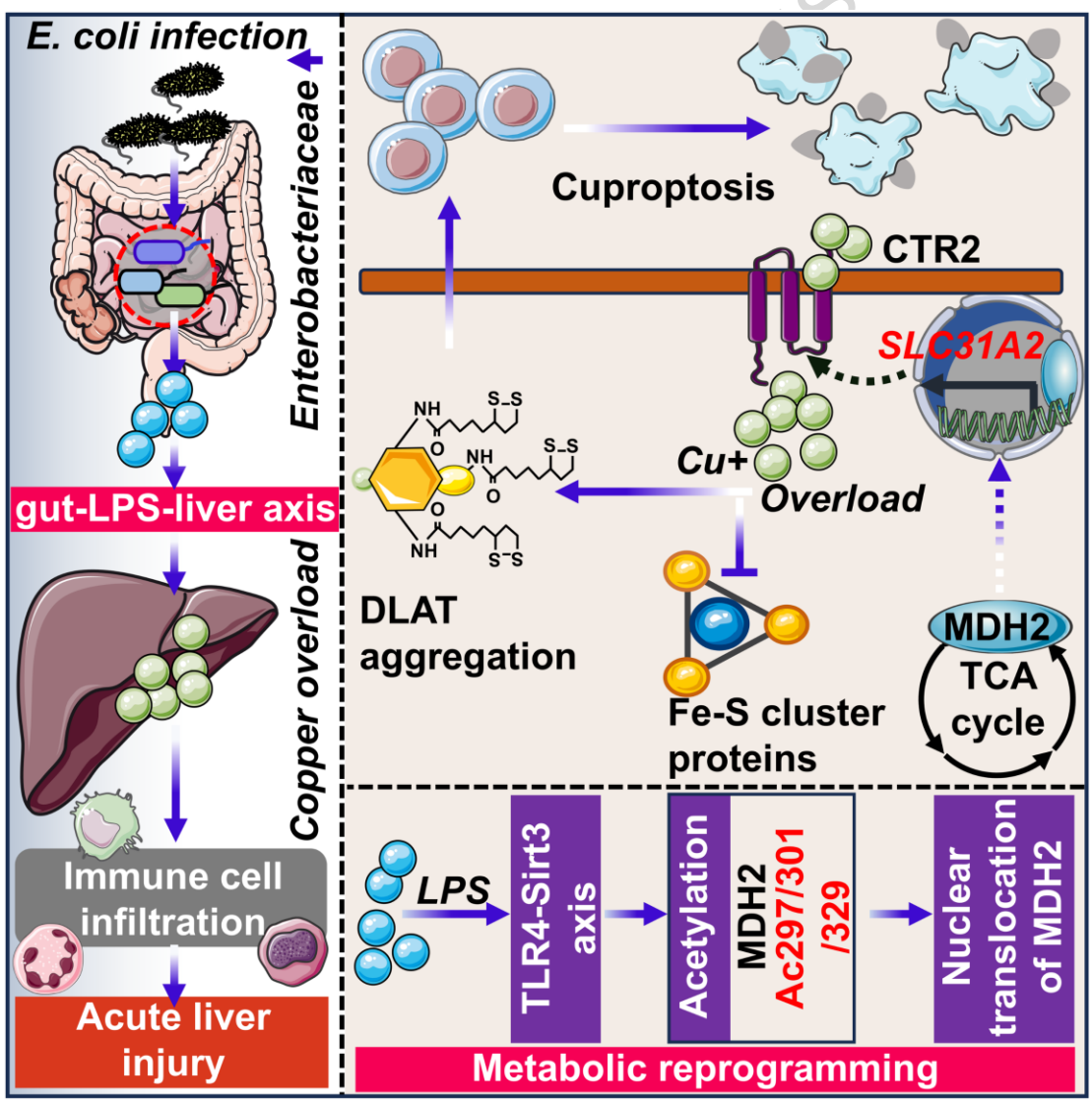
E. coli infection
Enterobacteriaceae
gut-LPS-liver axis
Copper overload
Immune cell infiltration
Acute liver injury
Cuproptosis
CTR2
SLC31A2
Cu+
Overload
DLAT aggregation
Fe-S cluster proteins
MDH2
TCA cycle
LPS
TLR4-Sirt3 axis
Acetylation
MDH2 Ac297/301/329
Nuclear translocation of MDH2
Metabolic reprogramming

Editorial Summary:

The study shows that E. coli infection disrupts copper balance by inducing CTR2 through acetylated mitochondrial MDH2, triggering cuproptosis and liver injury, and suggests that targeting this pathway may help limit infection-associated damage.

Peer Review Information: *Nature Communications* thanks Valerie J. Carabetta and the other anonymous, reviewer(s) for their contribution to the peer review of this work. A peer review file is available."